LUND UNIVERSITY

Growth of Semiconductor Nanowires for Solar Cell Applications

Heurlin, Magnus

2015

[Link to publication](#)

Total number of authors:
1

Growth of Semiconductor Nanowires for Solar Cell Applications

MAGNUS HEURLIN

DIVISION OF SOLID STATE PHYSICS | DEPARTMENT OF PHYSICS | LUND UNIVERSITY

Growth of Semiconductor Nanowires for Solar Cell Applications

Magnus Heurlin

Doctoral Thesis
2015

Division of Solid State Physics
Department of Physics
Lund University

Organization	Document name
LUND UNIVERSITY	DOCTORAL DISSERTATION
	Date of issue: October 26th 2015
Author: Magnus Heurlin	Sponsoring organization

Title: Growth of Semiconductor Nanowires for Solar Cell Applications

Abstract

Nanowires have the ability to absorb light much more efficient than conventional thin film layers. This makes them candidates for the development of new types of solar cells that have higher efficiency and lower material usage than current technologies.

In this thesis fabrication of nanowires with techniques suitable for large area applications are investigated. The nanowires are grown by either Metal Organic Vapor Phase Epitaxy (MOVPE) or a novel technique called Aerotaxy.

When using MOVPE nanowires are nucleated on a substrate. The position of nucleation can be determined with nanoimprint lithography by which several square centimeter surfaces can be covered with nanoscale patterns. The local environment will thus be similar for all nanowires during synthesis which is a prerequisite to achieve homogenous nanowire properties. During synthesis we have developed an optical technique to monitor the growth in situ. In situ monitoring can be used to precisely control the length of different sections, increase reproducibility, and achieve a better understanding of the complex nanowire growth process.

Aerotaxy grown nanowires nucleate from gold particles which are suspended in a stream of gas. This can increase the production rate substantially compared to substrate based techniques. By controlling the gold particle size and the reaction conditions in the growth chamber the nanowire properties can be tuned.

By incorporating a *p-n* junction within each nanowire it is possible to fabricate solar cell devices. We have connected two *p-n* junctions in series within a single nanowire by using a tunnel junction. This type of structure can in the future be used to achieve higher efficiencies of nanowire solar cells by implementing a multi-junction structure, with several sub-cells of different absorbing material. In a radial solar cell design carriers are extracted orthogonal to the direction of incoming light. With this geometry we could compare a vertical array device with that of a single nanowire device. With the array device an efficiency of 5.3% was achieved.

Key words	III-V semiconductor materials, nanowire, Aerotaxy, MOVPE, solar cells, photovoltaics	
Classification system and/or index terms (if any)		
Supplementary bibliographical information		Language: English
ISSN and key title		ISBN
		978-91-7623-506-5
Recipient's notes	Number of pages: 148	Price
	Security classification	

I, the undersigned, being the copyright owner of the abstract of the above-mentioned dissertation, hereby grant to all reference sources permission to publish and disseminate the abstract of the above-mentioned dissertation.

Signature _____ Date October 9, 2015

Growth of Semiconductor Nanowires for Solar Cell Applications

Magnus Heurlin

Doctoral Thesis
2015

Front cover: Scanning electron microscope image of an InP nanowire array grown from nanoimprint lithography defined gold particles. After growth, the gold particles were removed to prepare the sample for a shell growth step.

Intertek

FÖRPACKNINGS & TIDNINGS INSAMLINGEN

KLIMATKOMPENSERAT PAPPER

Contents

Abstract

Nanowires have the ability to absorb light much more efficient than conventional thin film layers. This makes them candidates for the development of new types of solar cells that have higher efficiency and lower material usage than current technologies.

In this thesis fabrication of nanowires with techniques suitable for large area applications are investigated. The nanowires are grown by either Metal Organic Vapor Phase Epitaxy (MOVPE) or a novel technique called Aerotaxy.

When using MOVPE nanowires are nucleated on a substrate. The position of nucleation can be determined with nanoimprint lithography by which several square centimeter surfaces can be covered with nanoscale patterns. The local environment will thus be similar for all nanowires during synthesis which is a prerequisite to achieve homogenous nanowire properties. During synthesis we have developed an optical technique to monitor the growth in situ. In situ monitoring can be used to precisely control the length of different sections, increase reproducibility, and achieve a better understanding of the complex nanowire growth process.

Aerotaxy grown nanowires nucleate from gold particles which are suspended in a stream of gas. This can increase the production rate substantially compared to substrate based techniques. By controlling the gold particle size and the reaction conditions in the growth chamber the nanowire properties can be tuned.

By incorporating a *p-n* junction within each nanowire it is possible to fabricate solar cell devices. We have connected two *p-n* junctions in series within a single nanowire by using a tunnel junction. This type of structure can in the future be used to achieve higher efficiencies of nanowire solar cells by implementing a multi-junction structure, with several sub-cells of different absorbing material. In a radial solar cell design carriers are extracted orthogonal to the direction of incoming light. With this geometry we could compare a vertical array device with that of a single nanowire device. With the array device an efficiency of 5.3% was achieved.

Populärvetenskaplig sammanfattning

Världen förbrukar i år ca 150 000 TWh energi. För att producera denna mängd energi skulle man behöva ca 40 miljoner vindkraftverk eller ca 6000 kärnkraftverk av Forsmarks storlek. Idag består världens energiproduktion till 80% av olja, kol och naturgas. Dessa fossila energislag har dock en negativ inverkan på miljön genom att släppa ut sot och växthusgaser som koldioxid (CO_2).

Solen är den största energikällan som finns i vår närhet. Den belyser varje timme jorden med en energimängd motsvarande 120 000 TWh. Detta motsvarar nästan människans årliga energiförbrukning. En solcell omvandlar energin i solljuset direkt till elektricitet. Under år 2014 producerades ca 200 TWh el från solljus så potentialen är enorm för detta energislag. Mängden el i världen som produceras från solceller växer nu i en exponentiell takt men nya innovationer krävs för att ökningen ska fortsätta. Det största hindret för ett större genomslag av solceller just nu är att priset för energin ofta är högre jämfört med andra energislag.

För att göra elektricitet producerad från solceller billigare kan man antingen öka deras verkningsgrad eller sänka kostnaden för att producera dem. Denna avhandling tar avstamp i båda dessa faktorer. I avhandlingen behandlas olika sätt att tillverka nanotrådar. Dessa nanotrådar är tunna avlånga kristaller och har en tjocklek som är ca 1000 gånger tunnare än ett hårstrå (se figur 1). Varje enskild nanotråd kan göras till en solcell. Genom att placera miljarder av dem bredvid varandra i en slags ”nanotrådsskog” kan man göra solceller som täcker tillräckligt stor yta för att vi ska kunna använda dem. Då man använder nanotrådar i en solcell kan mängden absorberande material minskas till ca 0.1% jämfört med en kommersiell solcell idag. Samtidigt finns det också en potential för att få högre verkningsgrad än dagens solceller.
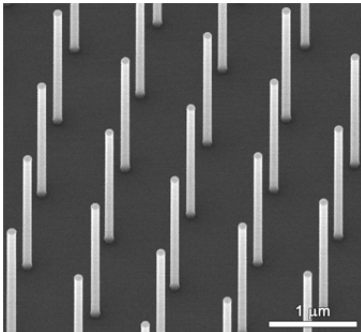

Figur 1. *Elektronmikroskopbild på rader av nanotrådar. Nanotrådarna står rakt upp från ett substrat och har ordnats i ett mönster genom att placera guldpartiklar på ytan med litografi. Från varje guldpartikel kan sedan en nanotråd växa.*

För att kunna tillverka alla dessa miljarder nanotrådar som behövs för att göra solceller som täcker stora ytor måste nya tillverkningstekniker tas fram. Dessa tekniker ska kunna framställa stora mängder nanotrådar med väldigt liknande egenskaper för att solcellen ska kunna göras så effektiv som möjligt. I denna avhandling har två tekniker undersökts för att framställa nanotrådar.

I den första tekniken används ett substrat på vilket nanotrådarna växer fram. Processen börjar med att små nanopartiklar av guld placeras på substratets yta. Växten påbörjas genom sätta in substratet i en växtkammare där temperaturen höjs till ca 450 °C samtidigt som man tillför gaser av materialen som nanotråden ska bestå av. Atomer från gasen når då guldpartiklarna där en kemisk reaktion gör att en fast kristall bildas. Själva nanotråden växer på detta sätt fram ett atomlager i taget under guldpartikeln. Genom att utveckla tekniker (litografi) för att placera guldpartiklar i mönster över en stor yta kan många nanotrådar tillverkas samtidigt. Med dagens teknik i vårt lab kan vi tillverka nanotrådar ståendes i ordnande mönster över flera kvadratcentimeter stora ytor. Detta motsvarar att vi kan tillverka i storleksordningen 1 miljard nanotrådar samtidigt. Mängden nanotrådar begränsas av storleken på substratet och storleken på växtkammaren.

I den andra tekniken tillverkar vi nanotrådar utan att använda ett substrat (se figur 2). Här förångas guld för att bilda nanopartiklar i en gas på liknande sätt som moln består av små vattenpartiklar som rör sig i luften. De små nanopartiklarna skickas, med hjälp av gasen som de rör sig i, genom en växtkammare där temperaturen höjs och växtmaterial tillförs. Trots att guldpartiklarna inte sitter fast på ett substrat kan nanotrådskristaller bildas och växa under guldpartiklarna. Nanotrådarna växer med denna teknik ca 1000 gånger fortare än på ett substrat och produktionstakten kan uppskattas vara ca 50 gånger större. Efter att nanotrådarna växt färdigt kan de deponeras på i princip vilket material som helst och där användas som t.ex. solceller.
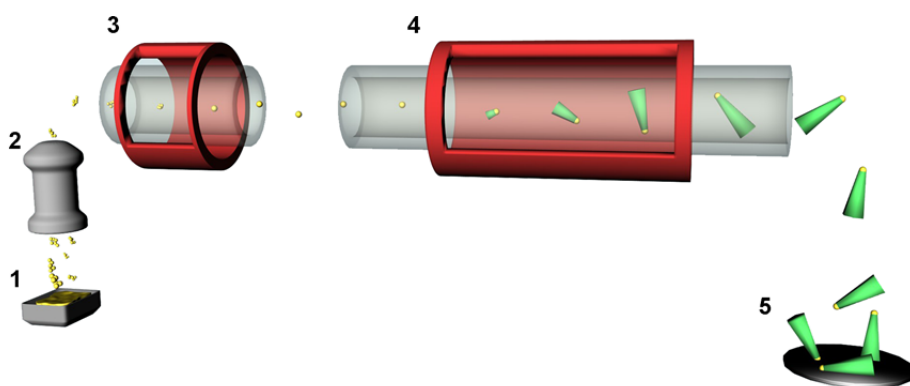
Figur 2. *Illustration av tillverkningstekniken Aerotaxi där nanotrådar växer utan ett substrat. Det börjar med att guldpartiklar förångas (1) och storlekssorteras (2). Efter detta skickas de genom en ugn för att få en jämn rund form (3) innan växtmaterial tillförs i växtkammaren(4) och trådarna bildas. Efteråt kan nanotrådarna deponeras på ett valfritt substrat (5).*

Acknowledgements

Although performing your PhD studies is sometimes a lonely task you realize that in order to make it all the way you need the support from friends, colleagues, and family. It is through the encouragement and help by these people that the achievements in this thesis were made possible.

I would first like to thank my principal supervisor Lars Samuelson who gave me an opportunity, first as a master student and later as a PhD student, to perform cutting edge research in the "nano world". Your innovative ideas and fantastic inspiration for the work we have done over the past few years has been invaluable. I am also thankful for the freedom you have given me to test my own ideas and satisfy my curiosity.

On a day to day basis I would not have made it through without the deep knowledge and endless source of ideas from Magnus Borgström. All our discussions throughout the years have helped me to develop as a researcher. You were never too busy when I came into your office, sat down in one of the chairs, and gave a small sigh because something didn't work out as I planned.

Even though not much TEM was included in this thesis I have spent numerous hours on this very cool instrument where you "see" the atoms. Reine Wallenberg has given me much knowledge and inspiration on this, both during my master and PhD studies. I always enjoyed when you came into the TEM room in the morning to chat a bit and see what I was up to.

The team working on growth of III-V nanowires for solar cell and LED applications in Lund has been growing over the past few years and I have enjoyed the company, discussions and collaborations with Gaute, Jesper, Alexander, Vilgaile, Xulu, David G, and Enrique. Together we can achieve more than on our own.

Over the years I have had close collaborations with many people who have turned my samples into something useful where we could actually measure something. Ali, Vishal and Reza, your tireless efforts with processing are admirable even though there were times where we felt that we should maybe give up. It has been a pleasure to work David L, Kristian, Olof, Bahram, Ofogh, Tomaš and Nicklas without whom I would not have gotten so much characterization of my nanowires and the science would have been much more boring.

I am thankful for the support from my parents Margareta and Anders who have given me a solid foundation to stand on and my sambos parents Åsa and Christer for all your help. Thanks to my sister and her family in Italy for all the fun moments, I hope you will move home soon.

Finally to the most important people in the world:

Ebbe, Tage och Camilla, ni är världens bästa familj. När vi är tillsammans förstår man vad som är viktigt här i livet. Jag älskar er.

Magnus Heurlin
Lund, October 2015

List of Papers

I.   **Continuous gas-phase synthesis of nanowires with tunable properties**

<u>M. Heurlin</u>, M. H. Magnusson, D. Lindgren, M. Ek, R. Wallenberg, K. Deppert, and L. Samuelson

Nature **492**, 90-94 (2012)

I performed the nanowire growth together with M.H.M, and most of the SEM and TEM analysis. I wrote the main part of the paper.

II.   **Axial InP Nanowire Tandem Junction Grown on a Silicon Substrate**

<u>M. Heurlin</u>, P. Wickert, S. Fält, M. T. Borgström, K. Deppert, L. Samuelson, and M. H. Magnusson

Nano Letters **11**, 2028-2031 (2011)

I developed the nanowire growth together with S.F., performed the TEM investigation and data analysis. I wrote the paper.

III.   **Optical Far-Field Method with Subwavelength Accuracy for the Determination of Nanostructure Dimensions in Large-Area Samples**

N. Anttu*, <u>M. Heurlin</u>*, M. T. Borgström, M-E. Pistol, H. Q. Xu, and L. Samuelson

Nano Letters **13**, 2662-2667 (2013)

*These authors contributed equally

I performed the nanowire growth and SEM measurements. I wrote part of the paper.

IV. **In Situ Characterization of Nanowire Dimensions and Growth Dynamics by Optical Reflectance**

M. Heurlin*, N. Anttu*, C. Camus, L. Samuelson, and M. T. Borgström

Nano letters **15**, 3597-3602 (2015)

*These authors contributed equally

I performed the nanowire growth and data analysis of the in situ measurements. I wrote the main part of the paper.

V. **Spatially resolved Hall effect measurement in a single semiconductor nanowire**

K. Storm, F. Halvardsson, M. Heurlin, D. Lindgren, A. Gustafsson, P. M. Wu, B. Monemar, and L. Samuelson

Nature Nanotechnology **7**, 718-722 (2012)

I developed the nanowire growth and took part in discussions regarding the results within the project.

VI. **Study of carrier concentration in single InP nanowires by luminescence and Hall measurements**

D. Lindgren, O. Hultin, M. Heurlin, K. Storm, M. T. Borgström, L. Samuelson, and A. Gustafsson

Nanotechnology **26**, 045705 (2012)

I took part in initiating the project, performed the nanowire and layer growth, and participated in discussions regarding the results.

VII. **Synthesis of Doped InP Core-Shell Nanowires Evaluated Using Hall Effect Measurements**

M. Heurlin, O. Hultin, K. Storm, D. Lindgren, M. T. Borgström, and L. Samuelson

Nano Letters **14**, 749-753 (2014)

I developed the nanowire growth, performed the TEM and SEM measurements, and interpreted the results. I wrote the paper.

VIII.   A Comparative Study of Absorption in Vertically and Laterally Oriented InP Core-Shell Nanowire Photovoltaic Devices

A. Nowzari, <u>M. Heurlin</u>, V. Jain, K. Storm, A. Hosseinnia, N. Anttu, M. T. Borgström, H. Pettersson, and L. Samuelson

Nano Letters **15**, 1809-1814 (2015)

I had an active role in planning of the project, developed the nanowire growth and wrote the part on nanowire growth in the paper.

Papers not included

The following papers are not included since they deal with topics beyond the scope of this thesis. They are listed in chronological order.

IX.   Nanowires With Promise for Photovoltaics

M. T. Borgström, J. Wallentin, <u>M. Heurlin</u>, S. Fält, P. Wickert, J. Leene, M. H. Magnusson, K. Deppert, and L. Samuelson

IEEE Journal of Selected Topics in Quantum Electronics **17**, 1050-1061 (2011)

X.   InAs quantum dots and quantum wells grown on stacking-fault controlled InP nanowires with wurtzite crystal structure

K. Kawaguchi, <u>M. Heurlin</u>, D. Lindgren, M. T. Borgström, M. Ek, and L. Samuelson

Applied Physics Letters **99**, 131915 (2011)

XI.   Growth of InAs/InP core-shell nanowires with various pure crystal structures

S. G. Ghalamestani, <u>M. Heurlin</u>, L. E. Wernersson, S. Lehmann, and K. A. Dick

Nanotechnology **23**, 285601 (2012)

XII.   **Reflection measurements to reveal the absorption in nanowire arrays**

N. Anttu, A. Iqbal, <u>M. Heurlin</u>, L. Samuelson, M. T. Borgström, M. E. Pistol, and A. Yartsev

Optics Letters **38**, 1449-1451 (2013)

XIII.   **Optical characterization of InAs quantum wells and dots grown radially on wurtzite InP nanowires**

D. Lindgren, K. Kawaguchi, <u>M. Heurlin</u>, M. T. Borgström, M. E. Pistol, L. Samuelson, and A. Gustafsson

Nanotechnology **24**, 225203 (2013)

XIV.   **Absorption of light in InP nanowire arrays**

N. Anttu, A. Abrand, D. Asoli, <u>M. Heurlin</u>, I. Åberg, L. Samuelson, and M. T. Borgström

Nano Research **7**, 816-823 (2014)

XV.   **III-V Nanowire Synthesis by Use of Electrodeposited Gold Particles**

R. J. Jam, <u>M. Heurlin</u>, V. Jain, A. Kvennefors, M. Graczyk, I. Maximov, M. T. Borgström, and L. Samuelson

Nano Letters **15**, 134-138 (2015)

XVI.   **Structural Properties of Wurtzite InP-InGaAs Nanowire Core-Shell Heterostructures**

<u>M. Heurlin</u>, T. Stankevic, S. Mickevicius, S. Yngman, D. Lindgren, A. Mikkelsen, R. Feidenhans'l, M. T. Borgström, and L. Samuelson

Nano Letters **15**, 2462-2467 (2015)

1 Introduction

On a yearly basis the world produces around 150'000 TWh of energy. The dominant source of energy is fossil fuels such as oil, coal and natural gas which account for more than 80% of the energy production [1]. In order to mitigate the effects of climate change and keep the temperature increase around 2 °C, emissions from these fossil fuels have to stop increasing in the near future, and instead start to decrease before the year 2050 [2]. Since the consumption of energy is expected to keep increasing, fossil free energy alternatives are needed for energy production.

Every hour the Earth receives 120'000 TWh of energy from the sun [3], which is comparable to the world's yearly energy production. Energy production from photovoltaics (PV) has been growing rapidly for the past 10 years and in 2014 around 200 TWh was produced which accounts for approximately 1% of the global electricity production (see Figure 1.1a).
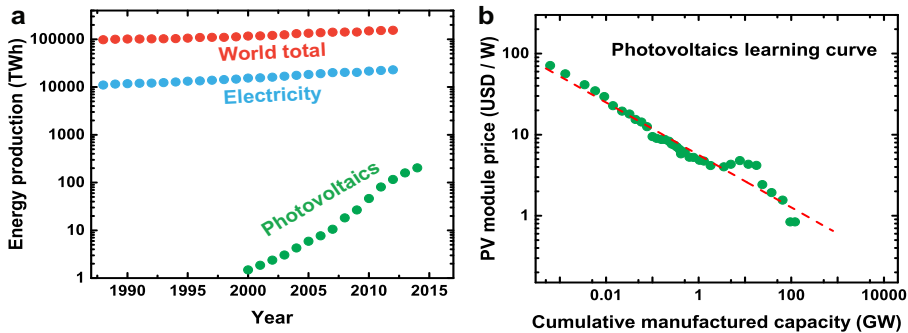
Figure 1.1 (a) Historic data of energy production in the world and in the form of electricity compared to the energy produced by solar cells. Data from ref. [1, 4, 5]. **(b)** Learning curve for photovoltaics showing expected price trend versus cumulative capacity. Data from ref. [6].

Price is one of the determining factors when considering which energy production source to use. Energy production from PV has undergone substantial price reductions as the cumulative manufactured solar cell capacity has increased (see Figure 1.1b). In 2009 the manufacturing cost of solar modules fell below 1 $/W [7] and is expected to reach 0.3-0.4 $/W by 2035 with a cumulative capacity of around 5000 GW [6].

Compared to other sources of energy, PV has a large potential for cost reduction which will lead to continued expansion of PV installations.

To compare the cost different energy sources one can consider the levelized cost of energy (LCOE). The LCOE takes into account the construction cost, capital financing, maintenance, incentives and possible fuel costs when operating an energy generating plant. In 2013 in Germany the LCOE of a fossil fuel power plant ranged from 0.04 – 0.10 €/kWh while LCOE of PV installations ranged from 0.08 - 0.14 €/kWh, which falls below the end-consumer price [8]. To describe when prices of energy generated by PV falls below the cost of buying it from the electric grid the term grid parity is used. As of 2013 grid parity had been reached in countries such as Australia, Germany, Italy and the Netherlands [6].

The drop in price of PV systems originates from more efficient manufacturing, lower material usage and higher conversion efficiencies. This has resulted in an energy payback time, i.e., the time it takes for a solar cell to supply the same amount of energy used to produce it, of between 1- 2 years for an installation in southern Europe [9].

To continue the learning curve shown in Figure 1.1b innovation is necessary which can ensure continued increases in conversion efficiency and lower material usage. Nanotechnology is likely to play a role in this strive and this thesis deals with how small rod like structures called nanowires can be used as solar cells. Nanowires have already been shown to provide high PV conversion efficiencies while keeping material usage as low as possible [10]. By taking advantage of the new possibilities offered by nanowires this thesis will show how they can be efficiently fabricated on large areas and be incorporated into functioning solar cell devices.

1.1 Nanowires

Semiconductor nanowires present a new way of producing different materials commonly used for electronic, photovoltaic and light emitting devices. Besides new ways of producing the active material, nanowires also offer new possibilities in controlling and tuning the material's physical and chemical properties. Nanowires themselves are typically rod like single crystalline structures which have a diameter from a few nanometres to a few hundred nanometres. Depending on the application their length usually varies in the range of 1 – 10 μm (see Figure 1.2). Their small dimensions place them in a regime where small changes in size or shape can have a large influence on the material properties [11]. They can be fabricated by either a top-down approach where a larger crystal is etched to form pillar structures or by a bottom-up approach where the nanowires are formed from material supplied through for example a vapour phase.

This thesis deals with bottom-up fabricated nanowires made from III-V semiconductor compounds which consist of elements from group III and V in the periodic table of elements. Most III-V materials have a direct bandgap which enables efficient absorption of photons in PV applications and efficient emission of photons in light emitting diode (LED) applications. Since it is possible to readily form alloys between different III-V materials it is also possible to tune the bandgap energy. Control of the bandgap energy enables tuning of the absorption range and emission wavelength in III-V semiconductor devices. This has proven to be important especially for high performance solar cells. Here materials with different bandgap are stacked on top of each other in order to convert as much energy in the sunlight as possible into electricity.
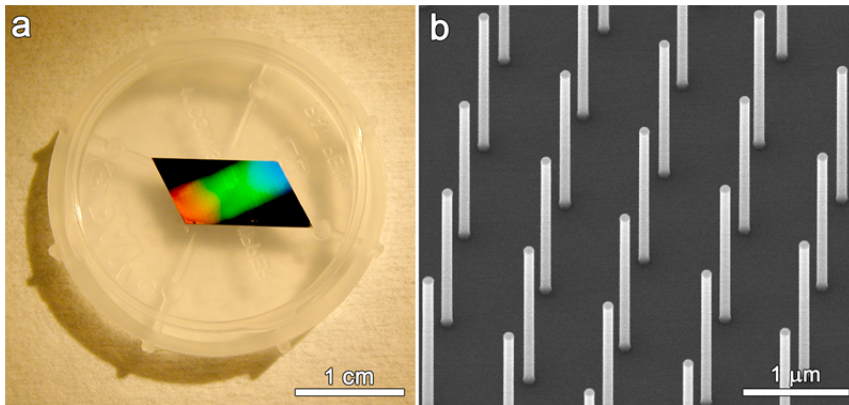

Figure 1.2 (a) Photograph of a sample with nanowires. The nanowires diffract the incoming light resulting in different colors which are visible. **(b)** Scanning electron microscope (SEM) image of the nanowires in (a) acquired at a tilt angle of 30°. The nanowires are standing vertically from the substrate and are roughly 100 nm in diameter. They are arranged in a periodic pattern with a nanowire-to-nanowire distance, or pitch, of 1 μm.

A challenge when combining different crystalline materials is that their lattice constant sometimes differs. This causes defects which leads to degradation of device performance. Due to the small footprint of nanowires strain at the interface between two materials with different lattice constant is reduced. This has enabled fabrication of nanowires with defect free lattice mismatched heterojunctions [12, 13] not possible to form in planar layers. Since it is possible to combine materials with different lattice constant it is also possible to integrate III-V nanowires on Si substrates [14]. This gives the possibility of implementing new functionality to Si based technology such as on-chip light emitters and detectors.

As will be discussed in the next chapter formation of nanowires largely depend on differences in surface energies which can be related to the atomic structure. Nanowires thus provide a feasible way of fabricating materials in a bottom-up fashion

with tailored properties. Extending the concept of nanowires beyond that possible with current planar technology, it has been shown that they can be grown as single crystals even without the use of a substrate to guide the growth [15](Paper I). This opens up even more exciting possibilities such as integrating inorganic semiconductors with soft materials, such as polymers. This could lead to substantial material and cost savings compared to today's leading technologies in the PV industry.

1.2 Outline of the Thesis

The aim of this thesis is to describe the fabrication processes needed to produce nanowires on a large scale which can be used in large area devices such as solar cells. Each chapter will start with an introductory part which describes the fundamental techniques, physics and material science necessary as background material for the topics that follow dealing with nanowires.

Chapter 2 describes the fundamentals of crystal growth and shows how this can be applied to understand why nanowires grow. It will give a description of three different nanowire growth techniques and show how the properties of the final structure can be tailored.

In chapter 3 aspects important when growing nanowires for devices are discussed, and especially how nanoimprint lithography can be used as a patterning technique for large area devices. Additionally, a method for measuring the size of nanowires while they are growing is described. This has the potential to give new insights in the nanowire growth process and improve process reliability. By the end of the chapter measurements of doping in nanowires and the effects of doping on the nanowire structure are discussed.

Finally in Chapter 4 two possible device structures for implementing nanowires as solar cells are discussed along with results on tandem junction structures and single junction core-shell structures.

2 Nanowire Growth Techniques

Over the last few decades nanowires have been grown by a several different techniques. This has ranged from techniques that operate in a solution to vapour phase techniques, such as chemical vapour deposition (CVD), and more physical techniques such as Molecular Beam Epitaxy (MBE). For a nanowire growth technique to be successful it must be able to produce high quality materials and be flexible enough to allow optimisation and formation of different layers, which is important for device fabrication. Growth of nanowires appears quite generic and can be accomplished both with and without seed particles. Choosing which technique to use can be based on the properties of the final structure. For example, by choosing a technique that does not employ a foreign seed particle material, formation of a homogeneous shell can be easier accomplished. On the other hand, by growing with a seed particle axial heterostructures can be fabricated with atomic precision.

In this chapter three different techniques to fabricate nanowires will be described. Before this some fundamental aspects of crystal growth are introduced. This forms a basis to understand the nanowire formation process in the different techniques. At the end of the chapter factors important for growing shells on the nanowires are discussed.

2.1 Metal-Organic Vapour Phase Epitaxy

Epitaxy originates from the Greek words *epi* - "above" and *taxis* – "in order". It relies on the use of a seed crystal, the substrate, upon which additional crystalline layers can be deposited. The atomic arrangement of the layers that are deposited is strongly influenced by the substrate. By choosing an appropriate temperature and supply of reactive species, it is possible to grow a crystal with a thickness increase of one atomic layer at a time.

The technique used to fabricate the samples in Papers II-VIII is termed Metal-Organic Vapour Phase Epitaxy (MOVPE) and is schematically outlined in Figure 2.1. It is today, together with MBE, the dominant technique for fabrication of high efficiency III-V semiconductor device structures. The applications where MOVPE is used are numerous and includes multi-junction solar cells [16], LEDs [17, 18] and lasers for optical communication [19].

MOVPE relies on the transition of material from a vapour phase into a crystal phase. In the vapour phase the atoms that should be incorporated are supplied in precursor molecules. The precursors can consists of low vapour pressure metal-organic molecules where, for example, a group III atom such as indium is bonded to three methyl groups and forms trimethylindium (TMIn). Group V atoms can be supplied in metal-organic form or as high vapour pressure hydrides, where a group V atom such as phosphorous is bonded to three hydrogen atoms and forms phosphine (PH_3). The overall reaction for the growth of InP using TMIn and PH_3 can thus be written as:

$$In(CH_3)_3 + PH_3 \rightarrow InP + 3\ CH_4.$$
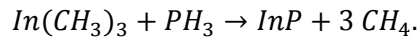
The growth process itself is very complex where the overall reaction is split into many parts and especially involves complex interactions with the surface of the crystal. The material quality of the deposited film is dependent on parameters such as input gas flows, temperature, reactor geometry and substrate contamination among others.
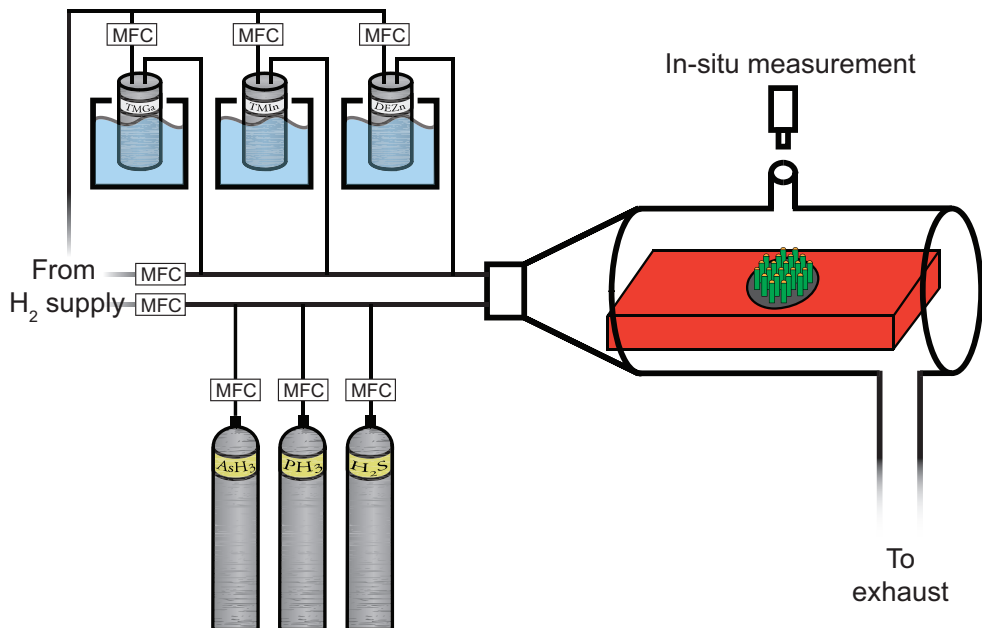
Figure 2.1 MOVPE system with three different metal-organic precursor sources placed in temperature controlled liquid baths and three high vapour pressure hydride sources supplied directly through gas bottles. The gas flows are controlled by mass flow controllers (MFCs). Inside the reactor the suceptor (red) is heated which together with the precursor molecules facilitates (nanowire) growth on the substrate. Above the reactor an in situ measurement tool is located which can aqcuire the optical reflectance spectra of the sample during growth.

2.1.1 Building a Crystal Atom by Atom

An intuitive description of crystal growth on an atomic level was first presented by Kossel [20]. In this description the incorporating atoms (adatoms) are viewed as building blocks which can move around on the crystal surface and later incorporate at preferential sites or desorb back into the vapour. The building blocks have six faces which can bind to other building blocks (see Figure 2.2). If a building block binds with more faces the bond becomes stronger and the overall free energy of the system is lowered.

The crystal growth process starts with an adatom (dark grey in Figure 2.2) that arrives from the vapour and adsorbs on the surface. At this stage the adatom is only weakly bound to the surface by van der Waals forces. The adatom is here said to be physisorbed and at this stage the available thermal energy is enough to break the temporary attractive forces enabling the adatom to diffuse on the surface or desorb. Incorporation into the crystal, or chemisorption, will occur once the adatom diffuses to a preferential site of incorporation such as an atomic step (yellow in Figure 2.2), kink (green in Figure 2.2), or step vacancy (blue in Figure 2.2). A third alternative is the formation of a nucleus (red in Figure 2.2) by several adatoms. This facilitates growth on an atomically flat surface.
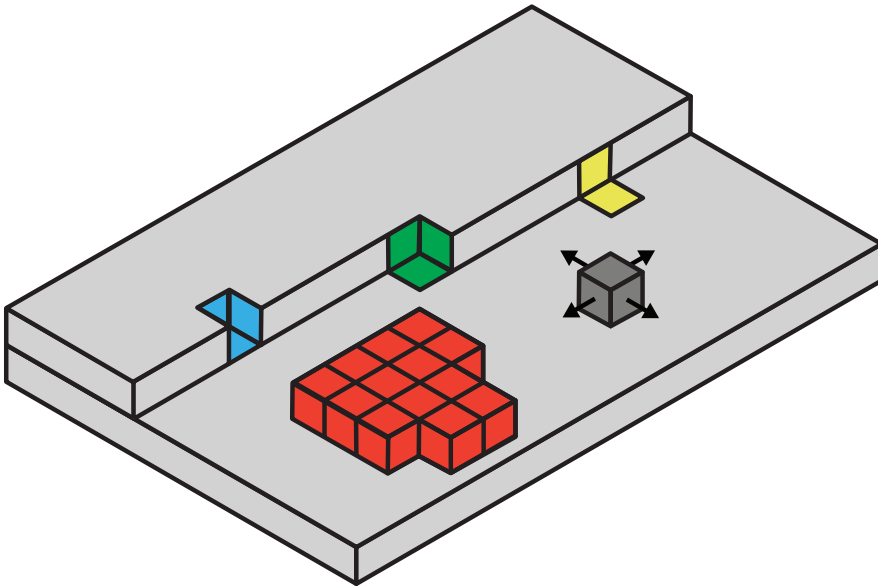
Figure 2.2 Crystal growth illustrated through building blocks. The adatom (dark grey) diffuses on the surface and can incorporate at the step (yellow), kink (green) or step vacancy (blue). The number of faces where the adatom can bind determines how strongly the adatom is bonded. If the diffusion length is smaller than the spacing between the steps, growth can proceed via a "birth and spread" mechnism where a nucleus (red) forms on the flat surface.

If incorporation of adatoms occurs mainly at atomic steps and kinks on the surface the growth is said to occur via a "step-flow" process where the atomic steps flow over the surface. The steps are thus moving perpendicular to the crystal growth direction. The growth substrate can be deliberately fabricated with many atomic steps by cutting it at a slight angle with respect to a low index plane, which facilitates this growth mode. If the adatom diffusion length is shorter than the distance between the atomic steps and the desorption rate is low, nucleation on the flat surface will dominate and growth proceeds via a "birth and spread" mechanism. Once a nucleus forms it will be similar to an atomic step and it will act as a preferential site for adatom incorporation.

2.1.2 Thermodynamic Driving Force

Epitaxy is ultimately controlled by thermodynamic laws which define if a crystal will grow, remain in its current state (equilibrium), or dissipate. Epitaxy involves at least two phases which can interact by exchanging energy (heat) and material (atoms or molecules). To keep track of the changes in energy and entropy of a phase, as material is exchanged, we can define the chemical potential of a phase as:

$$\mu = \frac{\partial G}{\partial N}_{T,P}.$$
(2.1)

In Eq. (2.1) μ is the chemical potential, G is Gibbs free energy and N denotes the material which is added or subtracted from the phase. The subscript T, P denotes that the transfer of material takes place under constant temperature and pressure.

The difference in chemical potential between the vapour phase (v) and the crystal phase (c) constitutes the thermodynamic driving force for crystal growth and can be expressed as:

$$\Delta\mu_{vc} = \mu_v - \mu_c.$$
(2.2)

If $\Delta\mu_{vc}$ is positive there is a driving force to move material from the vapour (high μ) to the crystal (low μ) phase and the crystal can grow larger. If $\Delta\mu_{vc}$ is instead negative the crystal (high μ) will lose material to the vapour (low μ) in an etching process. At equilibrium $\Delta\mu_{vc} = 0$ and there is no thermodynamic driving force to exchange material between the vapour and crystal.

By considering a simplistic system for epitaxy which consists of a monoatomic ideal gas in contact with a crystal of the same material the difference in chemical potential can be expressed as [21]:

$$\Delta\mu_{vc} = RTln\frac{P_v}{P_c}. \qquad (2.3)$$

Here R is the universal gas constant, P_v is the pressure of the ideal gas and P_c is the equilibrium vapour pressure of the solid crystal. The ratio P_v/P_c is called the supersaturation. Starting from an equilibrium situation, where $P_v = P_c$, an increase in P_v (from an external source of material) results in a positive $\Delta\mu_{vc}$, which constitutes a driving force for incorporating material into the crystal. By adding more material to the vapour $\Delta\mu_{vc}$ would increase further and thus give an even larger driving force for material deposition.

2.1.3 The Importance of Surfaces

Crystal surfaces are inherently different than the bulk crystal and are typically reconstructed in order to minimize their energy [22]. For small nanometre sized crystals, such as nanowires, the large surface to volume ratio results in a large influence of the surface on optical and electrical properties [23, 24]. For crystal growth the surface acts as the interface between the vapour and crystal phase and thus many processes are dependent on its state.

From the considerations in section 2.1.2 the process of crystal growth appears straightforward where the driving force and hence growth rate of a crystal is determined by how much material that is supplied. By only considering $\Delta\mu_{vc}$ we however remove the possibility of nanowire growth since the growth rate should be isotropic, i.e. constant in all crystal directions.

To account for that this is not the case we also need to consider how material can incorporate on a surface and how the energetics of the surface changes once new material is added [25].

For crystal growth to take place on a flat surface, atoms which arrive on the surface must form bonds to create a nucleus. A single atom or a small cluster of atoms would have a high energy due to many unsaturated bonds and tend to desorb. Considering the case of a two-dimensional nucleus with radius r and height h the change in G when the nucleus forms can be expressed as [21]:

$$\Delta G = -\Delta\mu\frac{\pi r^2 h}{V_{mc}} + 2\pi r\gamma. \qquad (2.4)$$

Here $\Delta\mu$ is related to the supersaturation on the surface, e.g. the number of adatoms compared to the equilibrium concentration, V_{mc} is the molar volume and γ is the energy related to the new atomic step that is formed by the nucleus. If $\Delta\mu$ is positive, promoting crystal growth, the first term describes the overall reduction in G when

adatoms are incorporated in the crystal phase. The second term describes the additional energy needed to create the new surface of the nucleus and will depend only on its perimeter in the case of homoepitaxy since the top surface will be the same as before the nucleus formed.

From Eq. (2.4) there is a balance between the energy gained when transferring material from a phase with high μ to a phase with low μ and the energy cost of creating a new atomic step. For small nuclei the $2\pi r \gamma$ term will dominate and lead to an increase in G ($\Delta G > 0$). However, for larger nuclei the $\Delta \mu$ term will dominate due to its dependence on r^2. The energy barrier after which an expanding nucleus will lead to a reduction in ΔG is called the nucleation barrier (ΔG^*) and can be expressed as [26]:

$$\Delta G^* = \frac{\pi \gamma^2}{\frac{h}{V_{mc}} \Delta \mu}.$$ (2.5)

Since γ depends on the surface upon which the nucleus forms different nucleation barriers can be expected on different crystal planes (see Figure 2.3) which will lead to different nucleation rates.
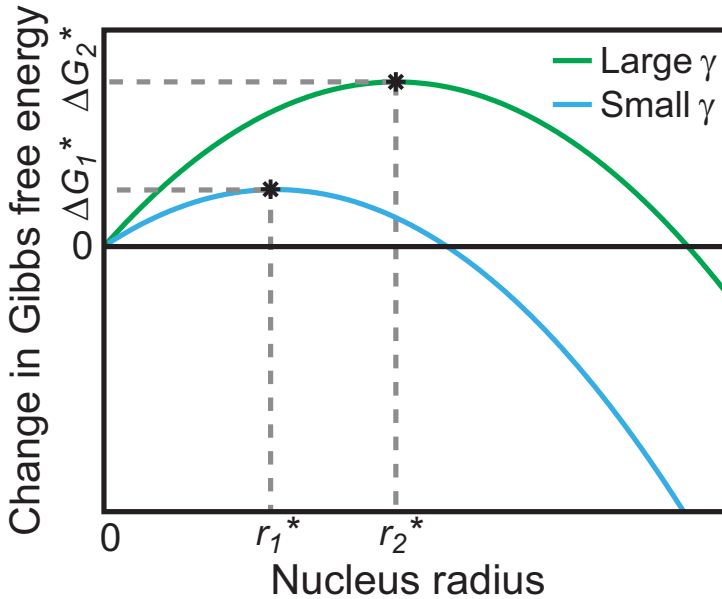

Figure 2.3 Nucleation barrier ΔG^* for different step energies γ. r^* indicates the critical radius after which continued growth is energetically favorable.

The shape of the nuclei will also be dependent on γ. Different step orientations will naturally have different atomic and bond arrangements and thus different γ. High energy steps will grow faster [27] and the resulting nucleus will typically have low index facets such as (001), (110) and (111).

2.1.4 The Effect of Growth Temperature

In the previous sections we have discussed how a driving force for crystal growth is established and how material can incorporate on a crystal surface. So far we have not considered how the growth material arrives on the surface and the processes which decompose the precursor molecules into the growth material and reaction by-products.

At low temperatures reaction kinetics will limit the growth rate [28] (see Figure 2.4). This will also impact the material quality of the epitaxial layers since, for example, unreacted carbon atoms can be incorporated. Several factors in the growth process are temperature dependent such as the decomposition of the precursors and hence the supersaturation. An excellent review of precursor decomposition is given by Stringfellow [29] and the general trends for TMIn, PH_3, trimethylgallium (TMGa) and arsine (AsH_3) are:

- The metal-organic molecules (TMGa and TMIn) decompose at lower temperatures than the hydride molecules (PH_3 and AsH_3).

- TMGa has a higher decomposition temperature than TMIn.

- PH_3 has a higher decomposition temperature than AsH_3.

- The decomposition temperature of AsH_3 and PH_3 is significantly lowered (up to several hundred Kelvin) when introduced together with TMGa or TMIn.

- The decomposition temperature of AsH_3 and PH_3 is significantly lowered in the presence of a GaAs or InP surface, respectively.

The complex processes which ultimately results in the presence of In, Ga, As, and P on the surface makes determination of the actual concentrations of growth species on the surface and at the growth interface difficult. It is however clear that incomplete decomposition of the metal-organic molecules leads to carbon incorporation that can lead to non-intentional doping and reduced carrier lifetimes.

Typical growth temperatures for 2-D layers are in the mass-transport limited regime and this also produces the highest quality material with for example low levels of carbon impurities. In this regime the growth rate is independent of temperature. The factor limiting the growth rate is instead material transport through the vapour phase to the growth interface.
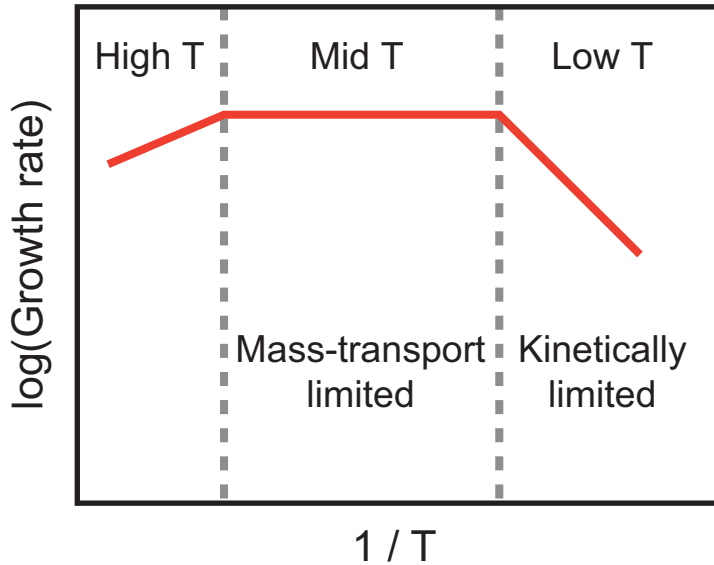
Figure 2.4 Logarithm of growth rate vs. inverse temperature for a typical MOVPE process. For low temperatures reaction kinetics limits the growth and an exponential increase in the growth rate with inverse temperature is obeserved. At medium temperatures the precursors decompose more readily and the growth rate is temperature independent. The growth rate is instead limited by supply of growth material. At very high temperatures the growth rate is reduced due to for example desorption of growth material from the crystal surface or parasitic reactions in the reactor.

Particle assisted nanowire growth typically takes place in the kinetically limited regime and material quality is thus of a high concern. Several studies of Au-seeded nanowires have however indicated that carbon incorporation, which reduces the material quality, mainly occurs in layer growth on the nanowire side facets [30-32]. It is thus probable that the Au particle either acts as a filter for undecomposed metal-organic precursors or as a catalyst which facilitates the precursor decomposition before incorporation.

2.2 Particle Assisted Nanowire Growth

Particle assisted nanowire growth has been successfully used to form nanowire structures that contain sharp axial heterostructures [12, 33-36], *p-n* junctions [37] (Paper II and IX) and well defined crystal structure transitions [38]. It is typically performed in the kinetically limited regime in order to limit growth on the nanowire side facets although higher temperatures can be used if for example an in situ etchant is introduced [31]. The following section gives an explanation to why nanowires can form and also discusses some important aspects of the growth mechanism.

12

Nanowire growth occurs in systems that contain an asymmetry which promotes growth at a certain location. This local enhancement of the growth rate can result in the formation of a one dimensional wire under the right growth conditions. By introducing nanoparticles on a substrate surface it is possible to locally enhance the growth rate underneath the particle thus promoting nanowire growth (see Figure 2.5). The use of particles to form wires was first investigated by Wagner, Ellis and Barns in the 1960s where metal particles (primarily Au) was used to form Si, GaAs and GaP wires [39, 40]. Many of the technologically important aspects of wire growth, such as *p-n* junctions, heterojunctions and growth from patterns, were suggested already in this early work.
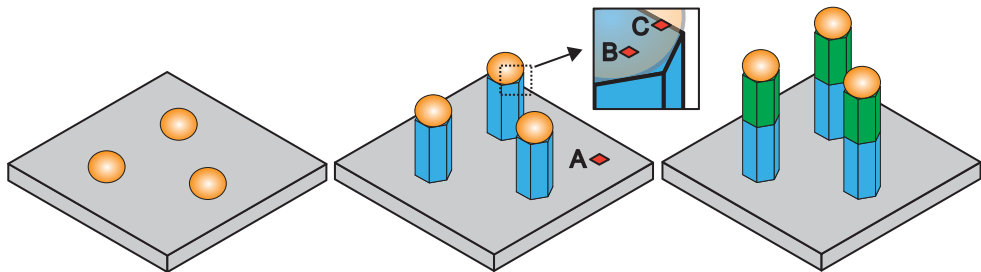

Figure 2.5 Schematic of the particle assisted nanowire growth process. First nanoparticles, typically Au, are placed on a substrate surface. Growth is initiated by the addition of material through the vapour phase. Different sites where nucleation of new crystalline layers can occur are marked as A, B, and C. By switching the precursors, which are supplied through the vapour phase, axial heterostructures or *p-n* junctions can be formed.

Wagner and Ellis originally proposed the vapour-liquid-solid (VLS) mechanism to explain why a wire could form underneath a particle. As the VLS name entails growth proceeds from the interaction of three phases in different states: a supply phase (vapour), a particle phase (liquid), and a crystal phase (solid). VLS gives a good description of the different parts required for wire growth to take place although later investigations have shown wire growth to be more general where the supply phase does not have to be a vapour [41, 42] and the particle is not always a liquid [43].

In order to find a general explanation to nanowire formation we first examine the thermodynamic driving force for crystal formation in a three phase system. The chemical potential of the vapour phase (μ_v) must be larger than or equal to that of the crystal phase (μ_c) and that of the particle phase (μ_p) since otherwise material would be transferred from the particle and/or the crystal to the vapour in an etching process. Additionally, since we observe growth underneath the particle μ_p must also be larger than or equal to μ_c. This gives the inequality:

$$\mu_v \geq \mu_p \geq \mu_c. \tag{2.6}$$

From Eq. (2.6) we can see that the largest driving force (defined as the difference in chemical potential between two phases) should exist between the vapour and crystal and would thus not promote a higher growth rate underneath the particle.

Next we consider the possibility of the particle acting as a catalyst for the decomposition of precursor molecules. If the precursor decomposition is locally enhanced, the concentration of growth material can be higher near the particle and thus a high μ could be found here. This approach is attractive since it would explain why particle assisted nanowires typically grow in the kinetically limited regime. However investigations have not given a clear answer if the presence of a particle lowers the activation energy compared to planar growth, which would be a clear signature of a catalytic process [44, 45].

Neither the difference in chemical potential nor catalysis by the particle can provide a general mechanism for nanowire formation. Instead the energetics that drives the nucleation of new crystalline layers should be considered [46-49]. The change in Gibbs free energy (ΔG) for an arbitrary nucleus forming on an atomically smooth facet at location A, B or C in Figure 2.5 can be written as [48]:

$$A: \Delta G_A = -\Delta\mu_{vc}n + Ph\gamma_{vc}$$

$$B: \Delta G_B = -\Delta\mu_{pc}n + Ph\gamma_{pc} \tag{2.7}$$

$$C: \Delta G_C = -\Delta\mu_{vc}n + P_{pc}h\gamma_{pc} + P_{vc}h\gamma_{vc}.$$

Here $\Delta\mu_{vc}$ and $\Delta\mu_{pc}$ is the difference in chemical potential per atom added to the nucleus at the vapour-crystal and particle-crystal interfaces and n is the number of atoms added to the nucleus, similar to the first term in Eq. (2.4). The second term in Eq. (2.7) contains the perimeter of the nuclei P, the height of the nuclei h and the step energies γ_{vc} and γ_{pc} at the newly formed vapour-crystal and particle-crystal interfaces, similar to the second term in Eq. (2.4).

Comparing expressions for ΔG at location A, B, and C and knowing that $\Delta\mu_{vc} \geq \Delta\mu_{pc}$ we find that ΔG can only be lower underneath the particle (location B and C) if the step energy at the particle-crystal interface is smaller than at the vapour-crystal interface i.e. $\gamma_{vc} > \gamma_{pc}$. This is likely since the interaction should be stronger between the particle and crystal than between the crystal and vapour, which would reduce the step energy. The most favourable location for nucleation to take place is at location C where all three phases (vapour, particle, and crystal) meet. At location C the supersaturation is highest and the shape of the nucleus can adjust to minimize the contribution from the step energies γ_{vc} and γ_{pc} [48].

Recently further refinements of nanowire growth theory have been made after experimental findings from in-situ TEM [50]. By observing nanowire growth in real

time a truncated facet at the vapour-particle-crystal interface has been observed. Thus the assumption of a flat particle-crystal interface is not always valid. Nucleation could then occur at the particle-crystal interface (location B) instead of the vapour-particle-crystal boundary (location C) as an extension of the truncated facet. In addition to this an oscillating behaviour of the truncated facet, directly related to the supersaturation in the droplet, indicates that growth occurs in a step-flow process where the supersaturation is reduced during layer formation but increases afterwards until the next layer nucleates [51].

To summarize, particle assisted growth of nanowires proceeds by a birth and spread mechanism where a new layer is nucleated and then grows in a step-flow manner. Nucleation of new layers is most favourable underneath the particle since here the step energy of the newly formed nucleus is lowest. The supersaturation of the particle oscillates periodically as it is depleted during layer formation but replenishes with growth material between nucleation events.

2.3 Selective Area Nanowire Growth

Selective area growth uses an inert mask template to define the position where epitaxial growth can take place. The method itself originates from the 1960s [52] and has for example been used to fabricate semiconductor laser structures [53] and transistors [54].

For nanowires, selective area growth is commonly used to fabricate single material structures (Paper IV) or core-shell heterostructures [55] and *p-n* junctions [56, 57]. A few reports exist for axially formed structures [58] although these are commonly associated with simultaneous shell growth [59]. Growth is typically performed in the mass transport limited regime and the following section will give an explanation to why they can form and general characteristics of the nanowire structures grown using this technique.

Nanowire growth without the use of a particle can be accomplished by adding an inert mask on top of a substrate through which holes are etched (see Figure 2.6). The hole diameter will, together with the amount of radial growth, determine the final nanowire diameter. Precursors containing the growth material are supplied through the vapour phase and reach the surface where pyrolysis and diffusion can occur, which transports growth material into the mask openings. To explain why a pillar like structure can form we can use similar arguments about the nucleation energetics as was presented for particle assisted nanowire growth. The change in Gibbs free energy (ΔG) for an arbitrary nucleus forming on an atomically smooth facet at location A, B or C in Figure 2.6 can be written as [48]:

$$A: \Delta G_A = -\Delta\mu_{vm}n + Ph\gamma_{vc} + A\sigma$$

$$B: \Delta G_B = -\Delta\mu_{vc}n + Ph\gamma_{side} \qquad (2.8)$$

$$C: \Delta G_C = -\Delta\mu_{vc}n + Ph\gamma_{top}.$$

Here $\Delta\mu_{vm}$ is the difference in chemical potential at the vapour-mask interface, A is the nucleus area and σ is the sum of interfacial energy associated with the vapour-crystal and crystal-mask interfaces. γ_{side} and γ_{top} are the step energies for a nucleus that forms on the side and top facets of the nanowire respectively.
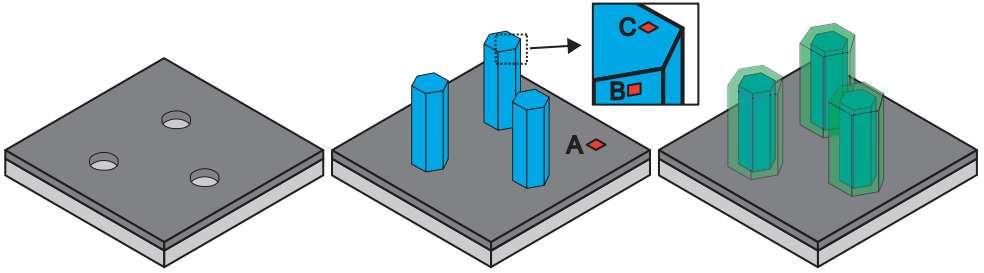

Figure 2.6 Schematic of the selective area nanowire growth process. First an inert mask material, through which holes are etched, is deposited on the substrate surface. Growth is initiated by the addition of growth material through the vapour phase. Different sites where nucleation can occur are marked as A, B and C. By switching the precursors which are supplied through the vapour phase, and other growth parameters such as temperature, heterostructures and *p-n* junctions in a core-shell geometry can be formed.

The possibility of a nucleus forming on the inert mask is very unlikely due to the extra energy cost of $A\sigma$. Growth material present on the mask either desorbs back into the vapour or diffuses to a nanowire where it can incorporate. The reason for nanowire formation lies in the difference between the step energies γ_{side} and γ_{top}. If γ_{side} is high nucleation will be suppressed here reducing the amount of radial growth and thus enabling nanowire formation. Due to the high step energy any step that forms on the side facet should propagate rapidly and thus form a structure with a very small amount of tapering [60].

2.4 Aerotaxy

The previously described nanowire growth techniques require a substrate to define the location of nanowire nucleation. The substrate also has a fixed orientation relative to the nanowires, where the preferential nanowire growth direction is [111]B for most materials. By using a substrate there is a built in limitation to how many nanowires that can be produced per unit time, determined by the finite size of the available growth substrate. Paper I shows a way to overcome this by using Aerotaxy. Here Au aerosol particles suspended in a carrier gas are used to define the nucleation point of each nanowire (see Figure 2.7). This circumvents the limitation of a finite substrate size and the nanowire production process becomes continuous.
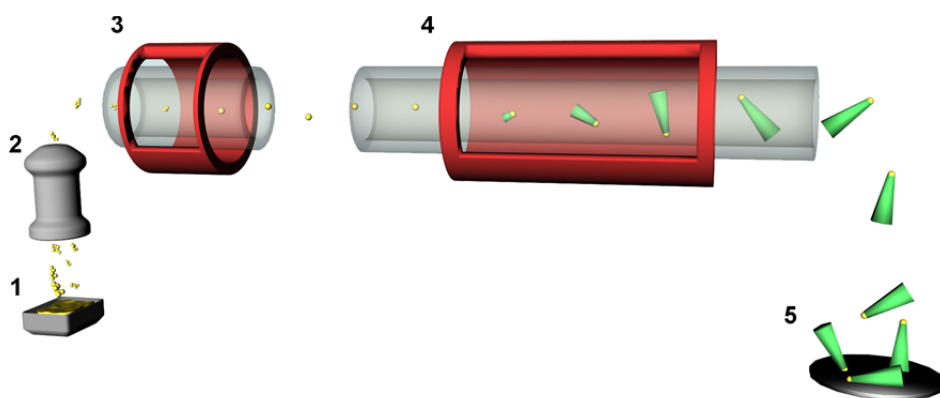

Figure 2.7 Overview of the Aerotaxy growth system with (1) Au agglomerate formation, (2) Au agglomerate size filtering, (3) Au agglomerate compaction to spherical particles in a sintering furnace, (4) nanowire growth after adding precursors to the aerosol and (5) nanowire deposition on a substrate.

Previous reports on gas phase nanowire growth techniques have been scarce except for the pioneering work performed by Charles Lieber's group in the late 1990s and early 2000s [15]. Here laser ablation, where a metal coated substrate is bombarded with high intensity laser pulses, was used to form large aspect ratio nanowires. The method itself appeared very versatile in terms of which materials that could be fabricated [61], but lacked control of the nanowire diameter and length.

Aerotaxy offers control of both the nanowire diameter and length by tuning the Au particle size and growth time as shown in Figure 2.8. Since the process is continuous the growth time is determined by the residence time in the hot part of the reactor. This can be changed by replacing the entire furnace for one with a longer hot zone or by changing the speed of the gas that carries the Au particles / nanowires.
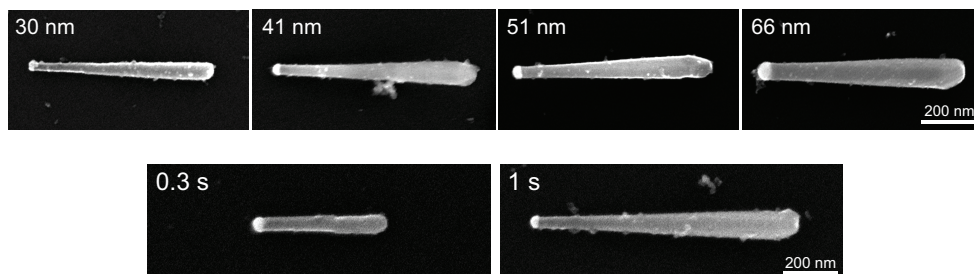
Figure 2.8 SEM images of Aerotaxy grown GaAs nanowires where the Au particle diameter (top) and growth time (bottom) has been changed.

The speed of the gas is controlled by the total gas flow and the cross-sectional area of the reactor tube. The simplest way to increase (decrease) the growth time is thus to either decrease (increase) the carrier gas flow or increase (decrease) the reactor tube diameter.

The Aerotaxy process has many similarities with an MOVPE process. The precursors that were used in Paper I are the same (TMGa and AsH$_3$) as one would typically use in substrate based MOVPE growth of nanowires or thin films. The temperature dependence of the growth rate (see Figure 2.9) is also very similar with a kinetically limted regime at low termpatures (below 550 °C). At higher temperatures the growth rate is constant indicating mass-flow limited growth. The shape of the nanowires can also be controlled by tuning the temperature (see Figure 2.9). Similar as in MOVPE the tapering, or side facet growth, increases with increased temperature.

Currently there is a large effort on continued development of Aerotaxy both from a material science and device integration perspective. Since the work on Aerotaxy presented here was carried out, the design of the rector has been upgraded which leads to smaller distributions in for example nanowire length. Combining different materials in the same nanowire by using sequential growth stages is also important for device integration. This was recently realized at Sol Voltaics [62] which are working with commercialization of Aerotaxy for solar cell applications. One of the key issues that remain to be solved is how billions of nanowires can be oriented and incorporated into a large area device with electrical contacts. If this challenge can be resolved Aerotaxy could make a large impact by producing high quality nano materials at a low cost.
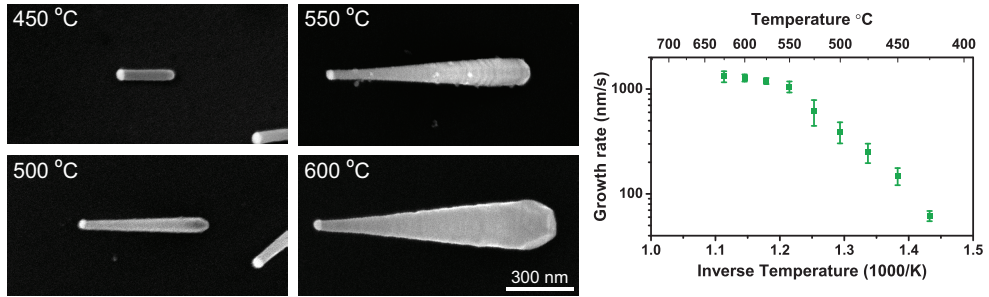
Figure 2.9 SEM images of GaAs nanowires grown by Aerotaxy at different temperatures (left) and the dependence between inverse growth temperature and growth rate (right). The temperature dependence of the growth rate indicates a kinetically limited regime below 550 °C.

2.5 Nanowire Polytypism

The stable bulk crystal phase of As, P and Sb based III-V materials is zinc blende (ZB) while for N based III-V materials it is wurtzite (WZ). However, nanowires of the As and P based materials used in this thesis commonly exhibit a mixture of both crystal structures [63] which affect their morphological, electronic [64] and optical properties [65].

The difference between WZ and ZB along the typical <111> nanowire growth direction is quite subtle. As can be seen in Figure 2.10 the stacking sequence changes from ABABAB… for WZ to ABCABC… for ZB[1]. Comparing the stacking sequence ABA (WZ) with ABC (ZB) we find that every third layer, which differs, is rotated by 60° in WZ compared to ZB. Besides the pure crystal structures shown in Figure 2.10 it is also possible to obtain mixtures of the two. The simplest example of this is the formation of a single twin plane in ZB which gives the stacking sequence ABCBA where C is the twin plane. One can then consider C to be a monolayer thick plane of WZ [66].

---

[1] Each layer A, B, and C is actually a bi-layer which consist of III-V atom pairs. In the TEM images in Figure 2.10 the resolution is not enough to resolve the individual atoms and each dot thus represents a column of III-V atom pairs.
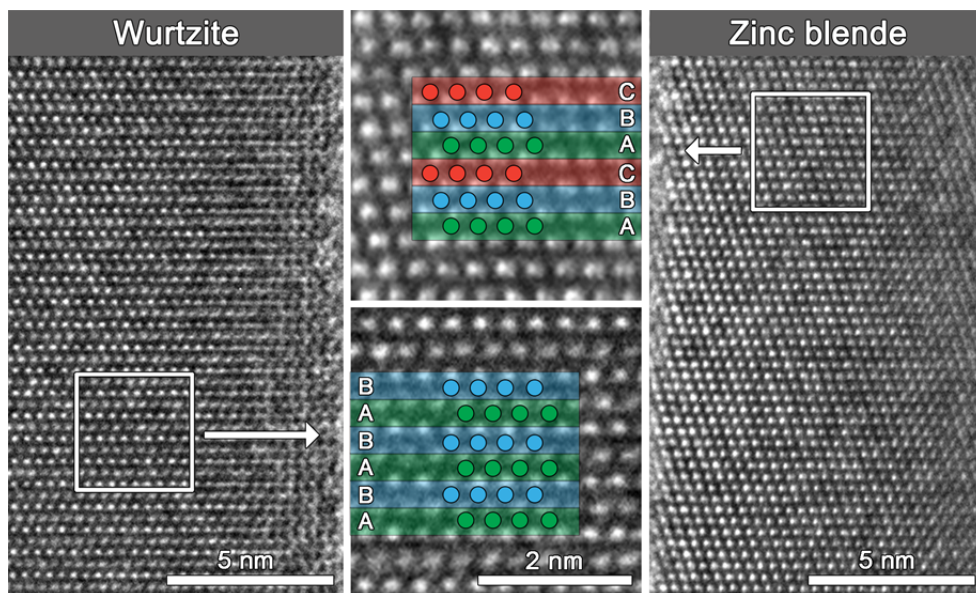
Figure 2.10 TEM images of WZ and ZB crystal structure where the imaged InP nanowires are oriented in the [$\bar{1}\bar{1}20$] direction for WZ and [$1\bar{1}0$] direction for ZB. The overlaid colours correspond to the layer stacking sequence ABABAB in WZ and ABCABC in ZB illustrated by the dots which indicate the location of In-P atom pairs.

In particle assisted synthesis of nanowires, the reason for WZ formation has been attributed to a lower step energy γ_{vc} of the WZ nucleus at the vapour-crystal interface. This reduces the WZ nucleation barrier when the nucleus forms at the vapour-particle-crystal interface (location C in Figure 2.5) [47]. This also correlates with the in-situ TEM observations that ZB GaP nanowires form when nucleation takes place underneath the Au particle (location B in Figure 2.5) as an extension of a truncated facet [50].

Growth parameters that affect the formation of WZ or ZB includes the group V flow [67, 68], the total precursor flow [69], growth temperature [32], particle size [70] and dopant flows [71, 72]. Throughout this thesis dopant flows have been used to control the crystal structure. This has proved to have large implications on for example shell growth [73](Paper X and XI). In addition, the crystal structure can also be used as an indirect signature of the magnitude of the doping level (Paper II). When using dopant flows to change the crystal structure of InP nanowires, Zn induces a ZB crystal structure with periodic twin planes, and S induces a WZ crystal structure. Sn on the other hand does not seem to have a large effect on the crystal structure of InP nanowires.

20

2.6 Shell Growth

Even though the growth rate in the nanowire growth direction is considerably higher than on the nanowire side facets, small amounts of shell growth is often present. The shell growth is in this case often of poor quality since growth parameters, such as temperature, have been optimized for axial nanowire growth. In this thesis HCl has been used as an in situ etchant to prevent this parasitic shell growth on the core nanowire [30]. For many device structures shell growth under controlled conditions is however desirable and thus much work have been put into optimizing this growth step.

Shell growth on nanowires has been used to fabricate structures with in situ surface passivation [74], radial *p-n* junctions [56](Paper VIII), remote doping [75] and quantized light emitters [76](Paper X and XIII). Shell growth requires the ability to switch growth modes from axial to radial growth, which can for example be accomplished by increasing or decreasing temperature or changing the V/III ratio [77, 78].

2.6.1 Influence of the Au Particle

Comparing nanowires grown by the particle assisted and selective area techniques, selective area nanowires have a distinct advantage in terms of shell growth. Since no metal particles are used during synthesis it is easier to grow core-shell nanowires with a good morphology, i.e., nanowires that have a uniform rod like shape. During shell growth of particle assisted nanowires the metal particle can act as a surface contaminant and influence the growth. For example, increasing temperature can result in the particle consuming the wire material in a reverse growth process (Paper XI). Additionally, since the particle can lower the nucleation barrier for new crystalline layers, growth underneath the particle can still be considerable [73] (see Figure 2.11a) even though growth parameters are no longer optimal for nanowire growth. Taking this into account leads to that growth parameters often need to be optimized to reduce the influence of the particle and not only improve the quality of the shell material.
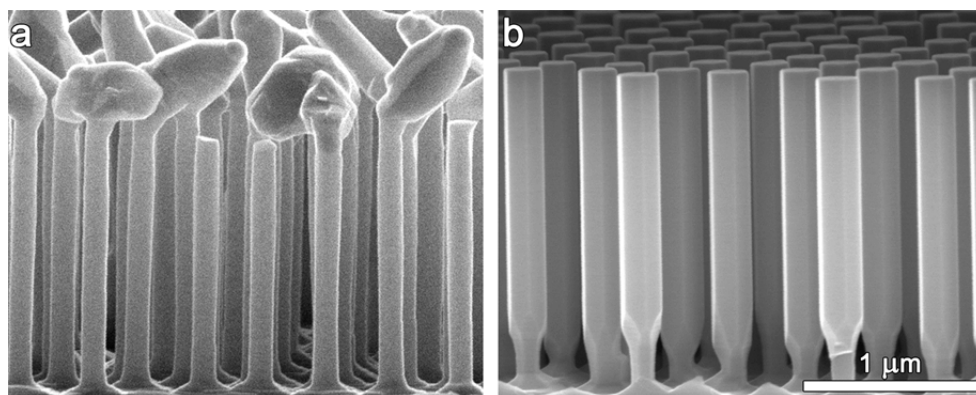
Figure 2.11 SEM images of core-shell InP nanowires grown under similar conditions. In **(a)** the Au particle was kept after core nanowire growth while in **(b)** the particle was removed and the shell was grown in a regrowth step. The shell was grown at a growth temperature of 550 °C while the core nanowire growth is optimized around a growth temperature of 400 °C.

In order to use core nanowires grown from particles, where extensive studies on doping and crystal structure exist, a method to remove the Au particle after growth was used [79](Papers V - VIII). This involved a wet etch step with a KI solution which etches Au selectively. After Au particle removal a regrowth step can be made (see Figure 2.11b), where growth of the shell material can be studied without influence of the Au particle. Using this hybrid approach it is possible to tailor the core structure to a larger extent than with selective area, and it is possible to optimize the shell growth in a wider parameter range than with particle assisted nanowires.

2.6.2 Effect of the Crystal Structure

When a shell nucleates on the side facet of a nanowire it will under most conditions adopt the same crystal structure as the core. This means that stacking defects present in the core will propagate into the shell. The crystal structure of the core nanowire can also have a large influence on the shell growth itself. In planar and selective area growth different substrate orientations can lead to differences in growth rate [27, 78], dopant incorporation [80] and ternary alloy composition [81]. Since WZ and ZB naturally have different surfaces similar effects would be expected. When investigating nanowire core-shell structures where the core consists of both pure WZ and pure ZB segments we found a higher shell growth rate on the ZB parts under many growth conditions (see Figure 2.12) [73, 82](Papers X and XI). From this, one can conclude that in order to obtain a smooth nanowire side facet, optimal for growth of 2-D shell layers, control of the crystal structure is important.
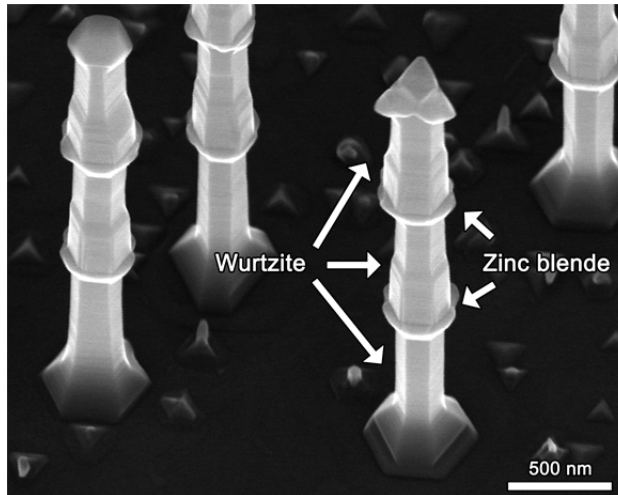
Figure 2.12 SEM image of a core-shell nanowire where the core consisted of pure WZ with two short (~50 nm long) ZB segments. The growth rate is enhanced on the ZB segments and on the WZ in the vicinity of the ZB segments.

Modulation of the crystal structure can however also be used in order to fabricate novel nanowire devices. By changing the crystal structure along the nanowire length quantum dot like structures can be formed on the ZB parts [83](Paper X).

2.7 Comparing the Three Growth Techniques

At this stage a comparison of the three growth techniques is in place. In general the different techniques have been developed and fine-tuned by different research groups. As the techniques develop further and hopefully become more well understood it will be possible to design and choose the suitable growth technique for each intended application. Since different research groups today are usually limited to one or two growth techniques also the number of possible structures and applications will be limited.

Table 1 gives an overview of the current status for some important aspects of the different growth techniques. Particle assisted nanowire growth has been restricted to those which are Au assisted since this is the most common particle material.

Table 1. Summary of current status for Au-assisted, Aerotaxy and selective area III-V nanowire growth techniques.

Growth Method	Au-assisted	Aerotaxy	Selective area
Control of diameter	Possbile with colloids, aerosols or lithography [84].	Similair limits as for aerosols deposited on a substrate [85](Paper I).	Possible with lithography [86].
Control of Shape	Depends on material diffusion [32] which is influenced by temperature [44] and precursor flows [87]. In situ etching is possible [88].	The shape depends on growth temperature (Paper I).	For InP it depends on crystal structure [68]. GaAs and InAs are typically rod like [89, 90].
Forming axial structures	Heterostructures [12, 33] and *p-n* junctions have been demon-strated [10, 91].	Not yet reported.	Some specific heterostructures possible [59]. *p-n* junctions shown for InGaAs [58] and GaAs [92].
Forming core-shell structures	Under certain conditions [24](Paper XI). Optimization needed to avoid Au particle influence for some materials.	Not yet reported.	Heterostructures [55, 59] and *p-n* junctions have been demons-trated [56, 57].
Control of crystal structure	Shown for InAs, InP, GaAs and GaP [93].	Typically zinc blende, twin density depends on temperature (Paper I).	Pure wurtzite shown for InP [68]. GaAs and InAs are typically mixed [94] or zinc blende with twin planes [95, 96].
Control of Doping	Quantitative studies exist for several materials including GaAs [97, 98] and InP [99].	*p*-type doping demonstrated for GaAs (ref. [100]).	Works qualitatively in devices [101, 102], quantitative studies are lacking.
Device fabrication	Several vertical device structures including transistor [103], solar cell [10] and LED structures [37] have been demonstrated.	Difficult, horizontal assembly of nanowires suspended in liquid possible with dielectro-phoresis [104].	Several vertical device structures including transistor [101], solar cell [57] and LED structures [105] have been demonstrated.
Process flow	Batch	Continous	Batch
Nanowire cost	Medium-High	Low	Medium-High

24

3 Nanowire Growth for Devices

For substrate grown nanowires to be useful in electro-optical devices such as solar cells and LEDs it must be possible to fabricate them on large wafer-scale areas. To achieve stable performance and high reproducibility it is also important to arrange the nanowires in a regular pattern so that each nanowire has a similar surrounding environment during fabrication. This ensures that variations in material properties between different nanowires are as low as possible. It also makes device fabrication (see Figure 3.1), where millions of nanowires should be connected in parallel, easier by ensuring that the spread in nanowire length and diameter is small. To characterise the length and diameter of nanowires in situ measurements can be used. This has the added benefit of continuously monitoring the evolution of the nanowire structure during growth. This further aids in establishing a reproducible process and gives a better understanding of the complex nanowire growth dynamics.

In this chapter the processes needed to fabricate nanowire arrays on large substrate areas are introduced. The basics of optical in situ measurements on nanowires are explained before the issues of doping and characterisation of carrier concentration in nanowires are discussed.
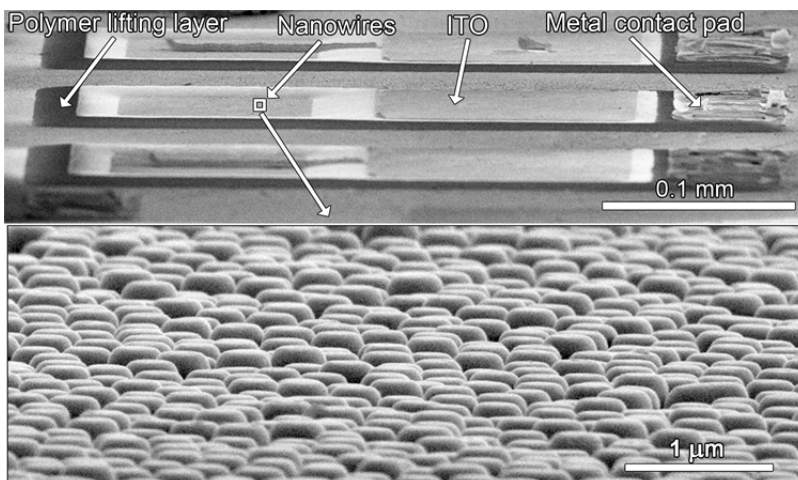

Figure 3.1 Side view SEM image of a nanowire device used in Paper VIII. A polymer lifting layer is used to avoid contacting nanowires outside of the device area. Bond wires or probes can be placed on the metal contact pad to make electrical measurements.

3.1 Nanoimprint Lithography

Nanoimprint lithography (NIL) provides means to replicate nano scale patterns with high precision over large areas while maintaining costs at a reasonable level. Nano scale patterns can be formed with a variety of techniques which all have their benefits and drawbacks. Self-assembly and bottom-up techniques, such as nanosphere lithography and block copolymers, are typically inexpensive and can provide a high pattern density but suffer from a lack of long-range order [106, 107]. In contrary standard top-down approaches such as electron beam lithography (EBL) and UV photolithography can provide excellent pattern replication, but become more expensive as the feature size decreases and the feature density increases. Moreover, the serial nature of EBL makes definition of large area patterns unfeasible if larger volumes of samples are required.

NIL can be used to bridge the gap between self-assembly methods and standard top down approaches by replicating small feature size patterns with high quality at a reasonable cost. Already in the first report of NIL the resolution was comparable to EBL [108] and has since then been scaled down even further [109]. Since the process is parallel, i.e., the entire pattern is formed in one step, it can be used to create patterns with high feature densities over large areas. By using NIL to either define Au particles on a substrate or holes in a growth mask it is possible to fabricate nanowires on large areas [110, 111].

3.1.1 Pattern formation

In this thesis work patterns formed by two different imprint technologies have been used. In Papers V, VI and VII patterns formed by substrate conformal imprint lithography [112] were supplied from MiPlaza. For Papers III, IV and VIII an in-house imprint process was developed, based on technology from Obducat [113], which is described in the following paragraphs.

Every imprint processes requires the formation of a master stamp which in this case was fabricated by using EBL and reactive ion etching (RIE) on a Si wafer. The stamp contains the pattern which should be transferred to the sample wafer. For the in-house developed process a copy of the Si master was made by electroplating Ni which results in a more flexible Ni stamp that can be used on a day to day basis. This step is used to prolong the lifetime of the Si master stamp which is expensive to fabricate. From the Ni stamp an intermediate polymer stamp (IPS) is made by imprinting an IPS plastic sheet into the Ni stamp in a thermal NIL step. During the imprint step a high gas pressure is applied to force the IPS polymer (which is heated above its glass transition temperature) to flow into the stamp pattern. The IPS has the same polarity

as the Si master stamp, i.e., if the master stamp consists of pillars so will the IPS. In contrary the Ni stamp has the opposite polarity and thus consists of holes in this case.

The III-V wafer (typically 2 inch diameter), which is to be imprinted, is spin coated with a double layer resist structure to enable lift-off. The first resist layer is a lift-off resist which is easily dissolved in a remover chemical while the second layer is an imprint resist into which the pattern is transferred. The remaining imprint process is shown in Figure 3.2. First a simultaneous thermal and UV (STU) imprint step, in which the IPS is placed on top of the III-V wafer, creates depressions in the imprint resist while leaving a small residual layer (see Figure 3.2a). The residual layer is removed by an O_2 plasma (see Figure 3.2b) before a wet etching step is used to partially etch the lift-off resist forming an undercut profile (see Figure 3.2c). Finally Au is evaporated (see Figure 3.2d) and since an undercut was formed a remover chemical which dissolves the lift-off resist can be used to remove the remaining resist and unwanted metal deposits. The formed pattern consists of Au discs (see Figure 3.2e) with a diameter determined by the imprint stamp and O_2 plasma step, and a height set by the thickness of Au evaporated. Since the nanowire diameter is determined by the volume of the Au disc it can be tuned to some extent for each stamp design by the O_2 plasma step and evaporated Au thickness. By reducing the Au thickness the resolution of the technique can be effectively increased and it is thus possible fabricate metal particles smaller than the feature size of the stamp [114]. The nanowire pitch is however fixed and determined by the master stamp.
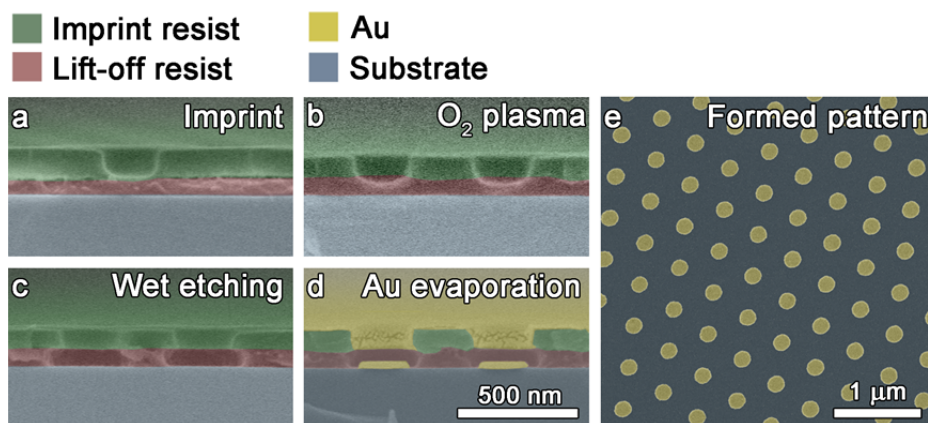
Figure 3.2 Overview of the in-house developed imprint process. **(a)** An IPS is used to form depressions in the imprint resist but leaves a small residual layer at the bottom of each hole. **(b)** An O_2 plasma is used to remove the residual layer before **(c)** a wet etching step creates an undercut profile. **(d)** Finally Au is evaporated and **(e)** a remover chemical is used to remove the remaining polymer and unwanted Au, leaving a regular pattern of Au particles.

For Papers IV and VIII an additional 20 nm thick layer of SiNx was also present on the substrate prior to imprinting. This is subsequently etched with RIE after the wet etching step but before Au evaporation resulting in a SiNx growth mask between the Au particles. For nanowires grown with the selective area technique presented in section 2.3 only the SiNx mask is used to define the nanowire positions and lift-off is performed after holes in the mask have been etched without deposition of Au.

3.1.2 Nanowire Growth from NIL Patterns

Nanowire growth from imprint patterns defined with the in-house process described in the previous section has been successfully accomplished for pitches ranging from 400 nm to 1 μm, and nanowire diameters ranging from 60 nm to 200 nm (see Figure 3.3 for examples). The formation of nanowires in pre-defined patterns is the basis for vertical nanowire devices. Nanowires arranged in regular a pattern all have the same local environment during growth which ensures that their properties, such as length and doping level, will be as similar as possible. From SEM measurements of NIL grown nanowires the standard deviation in nanowire length has been measured to be less than 1% [115] (on the order of 10's of nm), while the diameter spread is typically below 4% (about 2-5 nm for a 130 nm diameter nanowire)(Paper III). For small sample sizes the nanowire length can still vary considerably over the sample area due to edge effects which result in a different influx of material close to the sample edges. This effect was clearly visualised in Paper III where the nanowire length and diameter was mapped across millimetre sized sample areas.

The yield of nanowires grown from imprint patterns can vary and will depend on processing and growth conditions. In our lab it is possible to produce nanowire arrays with more than 99% yield on a routine basis and the best produced arrays have a yield above 99.8%. The defects which can appear are however important to understand so they can be eliminated, especially those which tend to be harmful for device fabrication.
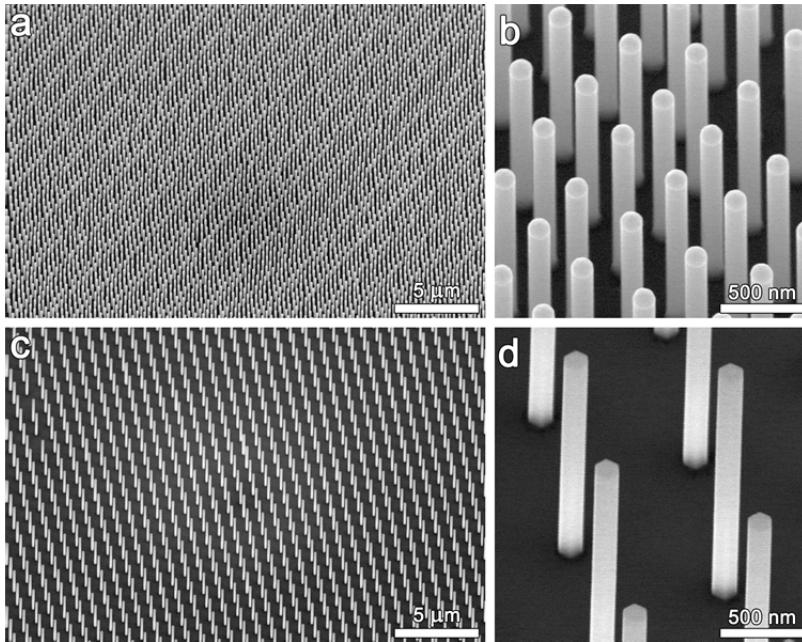
Figure 3.3 Nanowire growth from imprint patterns defined using the process described in section 3.1.1. **(a)** and **(b)** shows Au nucleated InP nanowires with a pitch of 400 nm and a nanowire diameter of 130 nm while **(c)** and **(d)** shows selective area grown InP nanowires with a pitch of 1 μm and a diameter of 145 nm.

Defects in nanowire growth from NIL patterns can be due to several factors.

1. Missing particles from the imprint process (see Figure 3.4a).
2. Thin nanowires growing in-between the intentionally positioned nanowires (see Figure 3.4b).
3. Non epitaxial nanowire growth due to failed nucleation (see Figure 3.4c).
4. Larger diameter nanowires accompanied by missing nanowires (see Figure 3.4d).
5. Many small nanowires growing in a position designated for one nanowire [115, 116].

Figure 3.4 Defects in nanowire growth from nanoimprint defined Au particles. **(a)** Top view after imprint showing missing particles due to the imprint process. **(b)** Formation of thin nanowires (indicated by arrows) in-between the larger intentionally grown nanowires. **(c)** Failed nucleation of a nanowire. **(d)** Larger diameter nanowires formed due to Au particles merging which also results in missing nanowires. Inset shows a top view of a similar area where some Au particles have merged before growth started.
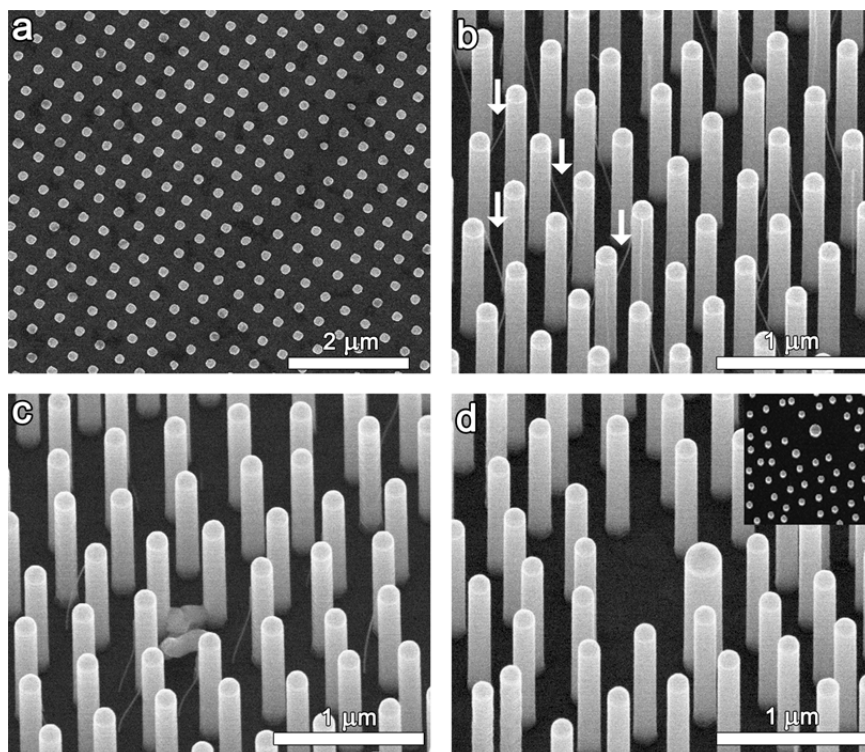
Missing particles from the imprint process is most often related to the quality of the imprint stamp. It is enough that a pillar of the IPS stamp is a few tens of nm's shorter than designed for the residual layer of imprint resist to not be penetrated during the O_2 plasma etch step (see Figure 3.2). If the residual layer is not penetrated it will not be possible to reach the substrate during the wet etch step and thus no Au can be deposited on the substrate.

Thin nanowires can either originate from small parasitic metal particles or from organic residues on the substrate surface [115, 117]. Organic contamination on the surface is actually a well-controlled way to form nanowires on for example a Si substrate [118]. These defects can be removed by optimization of the actual imprint process and will depend on the polymers used during imprint (especially those in contact with the substrate), the lift-off process and any potential cleaning procedure. For example when PMMA is used as the polymer in the lift-off layer it is essential to

use a piranha (mixture of H_2SO_4 and H_2O_2) etch step to remove polymer residues after imprint [115]. However, for the LOR resist employed throughout this thesis no such aggressive cleaning step was necessary and instead only an organic remover and water could be used for cleaning to achieve high yield patterns (see Figure 3.3).

Non-epitaxial nanowires can originate from a too low annealing temperature prior to growth or if organic residues are present at the Au particle-substrate interface. If the annealing temperature is too low oxides that reside on the substrate surface are not removed which prevents contact between the Au particle and substrate necessary for epitaxy.

Larger diameter nanowires originate from the movement of Au particles prior to nanowire nucleation. This problem is typically encountered when dense patterns with large Au particles are used. Once an Au particle has merged with another it appears that it is easier to merge with even more particles. As a result it is typically seen that many nanowires retain their diameter as defined by the imprint pattern while a few nanowires are grown from several merged Au particles (see Figure 3.4d inset). Early results indicate that the processing during imprint can affect the epi-ready oxide on the substrate surface which can result in Au particle movement [119].

Finally, the use of a too thin Au layer can lead to formation of many small nanowires in positions designed for one larger. If the Au layer is too thin it will break up during annealing due to surface tension, similar to a thin Au film [116]. This effect sets a limit on how thin nanowires that can be produced for each given imprint stamp, since the Au disc diameter has a lower limit set by the imprint stamp.

3.2 In Situ Measurements of Nanowire Growth

MOVPE is often considered as a "black box" where a sample goes into the reactor, certain growth parameters such as temperature and precursor flows are programmed, and the result is inspected afterwards. If the result was not as desired a new growth run with a new set of parameters is performed and this continues in an optimisation cycle. Finally, after enough optimisation cycles, a satisfying result is obtained which can be used for device processing and measurements.

A first step away from the black box approach is to formulate models which describe the growth result as a function of input growth parameters [120-122]. For nanowire growth several models exist which deal with mass transport [123, 124], alloy composition [125] and heterostructure formation [126]. These models often provide a way to interpret the growth results, but it can still be difficult to predict the outcome of a growth experiment since the models cannot incorporate all variables which control the growth. In addition developing and verifying the models are time consuming since it often requires many experiments.

In order to evaluate growth results faster, and obtain more details on the growth mechanism, in situ measurements can be used. For planar epitaxy using MOVPE, in situ measurements using optical techniques can be applied to determine the surface reconstruction, growth rate and alloy composition [127, 128]. For nanowires, in situ studies in a CVD process (like MOVPE) are however scarce [129], and most in situ studies have been performed in a high vacuum environment [130-132].

From Paper III, where the wavelength dependent reflectance signal of a grown nanowire array was studied, it was found that specific signatures existed in the reflectance spectra which were related to the nanowire length and diameter. Specifically it was found that:

1. Minima and maxima appeared in the wavelength dependent reflectance spectra due to constructive and destructive interference between light reflected at the nanowire-air and nanowire-substrate interfaces.

2. Absorption resonances appeared that were diameter dependent.

3. A larger diameter nanowire gave rise to more reflection at the nanowire-air interface than a thinner nanowire.

In Paper IV these basic concepts were used to develop in situ measurements of the nanowire length and diameter, which did not require computationally intensive 3-D modelling. Figure 3.5 provides an overview of the in situ reflectance data obtained from two different NIL patterns where the interference fringes and absorption resonances, used to identify the nanowire length and diameter, are explicitly shown.
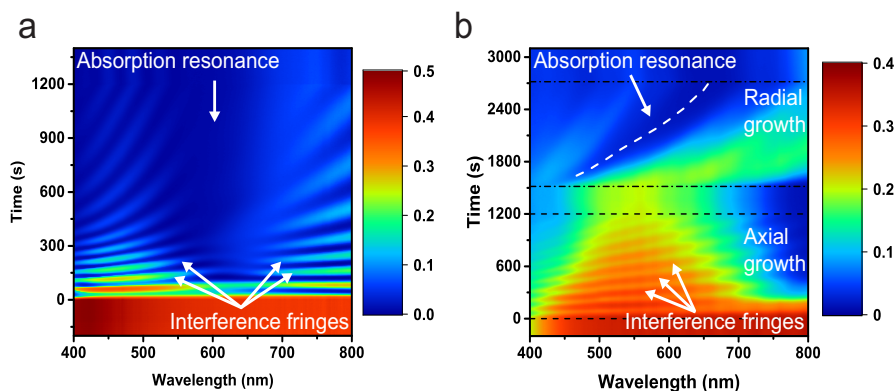
Figure 3.5 Colorplot reflectance spectra obtained from a Laytec EpiR DA UV optical reflectance tool connected to an Aixtron 200/4 MOVPE reactor during growth. **(a)** Reflectance spectra from axial growth of 130 nm diameter particle assisted InP nanowires with 400 nm pitch as defined by NIL. **(b)** Reflectance spectra from core and shell growth of selective area InP nanowires with a pitch of 1 μm as defined by NIL. During growth, axial elongation of the nanowires results in the appearance of interference fringes while radial growth causes a shift of absorption resonances.

3.2.1 Analysis of Axial Nanowire Growth

The axial growth of nanowires can be measured by analysing the interference between light reflected at the nanowire top and nanowire-substrate interface. Interference occurs because there is an optical path length difference (x_{OPL}) between light reflected at these two points given by:

$$x_{OPL} = 2Ln_{eff}. \tag{3.1}$$

In Eq. (3.1) L is the nanowire length, n_{eff} is an effective refractive index and the factor 2 originates from that light reflected at the nanowire-substrate interface has to make a round trip through the nanowire layer. For destructive interference x_{OPL} should be half a wavelength and for constructive interference x_{OPL} should be one wavelength. From this we can describe the minima and maxima that will arise for a specific wavelength as:

$$m\frac{\lambda}{2} = x_{OPL} \Longleftrightarrow L = \frac{m\lambda}{4n_{eff}} \quad m = 1, 2, 3, 4 \ldots \tag{3.2}$$

Here λ is the wavelength and m is an integer where every odd number (1, 3, 5…) gives a minimum in the reflectance signal and every even number (2, 4, 6…) gives a maximum in the reflectance signal. During a growth run L will increase and when the condition in Eq. (3.2) is met a minimum/maximum occurs. This can be verified by studying reflectance data at a single wavelength as seen in Figure 3.6a (equivalent to a vertical slice in Figure 3.5a).

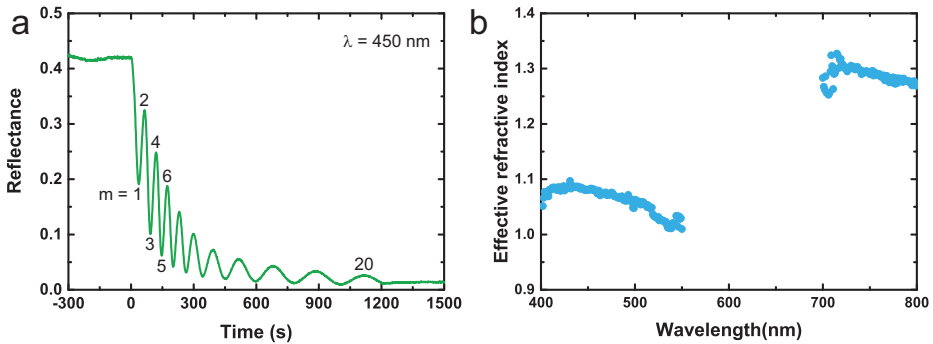**Figure 3.6 (a)** Reflectance signal at $\lambda = 450$ nm from a nanowire growth run where some minima and maxima have been marked with their respective m number. Growth starts at t = 0 s. **(b)** Effective refractive index n_{eff} of a nanowire array with 400 nm ptich and 130 nm nanowire diameter. Between 550 nm and 700 nm an absorption resonance exsists which makes extraction of n_{eff} difficult.

To extract the nanowire length L it is necessary to also determine n_{eff} which describes the interaction between the light wave and the nanowire layer. A reliable way to determine n_{eff} is to measure it for the specific nanowire array one wants to study. For this, a growth run is performed where a nanowire sample (with a certain nanowire pitch and diameter) is measured with both the in situ reflectance setup and SEM. By knowing L from SEM Eq. (3.2) can be rearranged to extract n_{eff} for those wavelengths where the growth ended precisely on either a minimum or a maximum. To extract n_{eff} for the remaining wavelengths, where the condition in Eq. (3.2) is not met, it is possible to perform a linear extrapolation, where one assumes a constant growth rate, from the last measured minimum and maximum to the point where the growth ends and thus add a fraction to m. This enables extraction of n_{eff} over the entire wavelength interval where interference fringes are visible (see Figure 3.6b).

To increase the temporal and spatial resolution of the in situ length measurement it is possible to employ a range of wavelengths. Adjacent wavelengths will for example reach their first maximum at slightly different nanowire lengths (see Figure 3.7). By using a wavelength range that contains 50-100 different wavelengths it is possible to achieve nearly continuous monitoring of the nanowire length, even though the growth rate changes in a non-linear fashion. Due to the high temporal resolution the growth rate itself can also be extracted as the derivative of the measured nanowire length vs. time data.
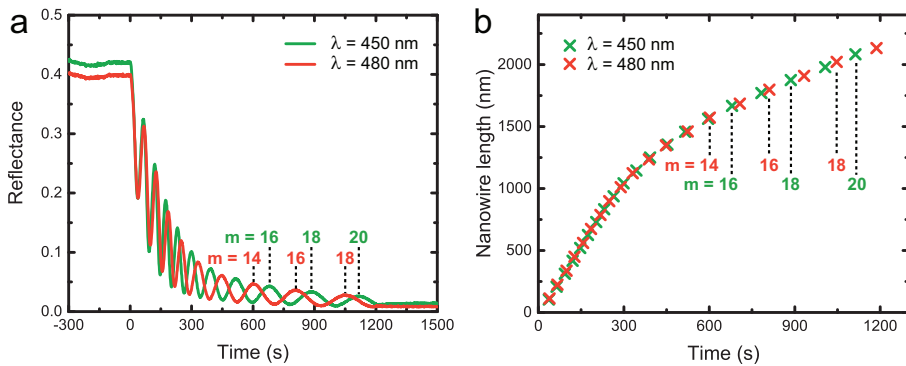
Figure 3.7 (a) Reflectance vs. time for λ = 450 nm and λ = 480 nm. Growth starts at t = 0 s. **(b)** Minima and maxima from (a) converted into nanowire length as a function of the growth time by using Eq. (3.2) and the n_{eff} displayed in Figure 3.6b. Some even m numbers have been marked and the data points in (b) can be directly correlated to the maxima in (a).

3.2.2 Analysis of Radial Nanowire Growth

The radial growth of nanowires can be measured by analysing the absorption resonances which are directly connected to the nanowire diameter [133, 134]. From modelling it was possible to extract the wavelength dependence of the two optical

modes which account for the strongest absorption resonances, denoted HE_{11} and HE_{12}, for different InP nanowire diameters (Paper IV).

$$D_{HE_{11}} = 0.95 \cdot \frac{\lambda - 173\ nm}{4.1} \qquad D_{HE_{12}} = 0.95 \cdot \frac{\lambda - 218\ nm}{1.45} \qquad (3.3)$$

The factor 0.95 in Eq. (3.3) accounts for that the nanowire cross section is hexagonal and not circular as used in the modelling. When the HE_{11} or HE_{12} are excited light strongly couples into the nanowire and thus enables a high absorption. To determine the nanowire diameter one only needs to find the wavelength which corresponds to the resonance in the reflectance data. This is easiest to accomplish when the interference signal is not too strong since then it will simply be the minima in the wavelength dependent reflectance spectra as seen in Figure 3.8 (equivalent to horizontal slices during shell growth in Figure 3.5b).

Since it is possible to measure one reflectance spectra each second the shell growth can be continuously monitored. This opens up for advanced design of core-shell structures where the thickness of each shell can be precisely controlled.
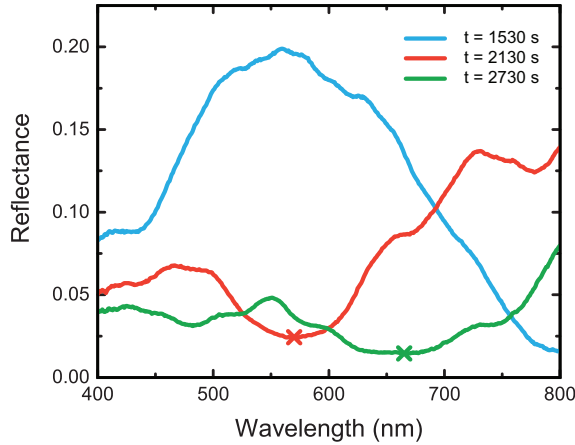
Figure 3.8 Wavelength dependent reflectance spectra during different stages of shell growth extracted from the data in Figure 3.5b, where minimum values used for identifying the nanowire diameter have been marked. The nanowire sample consisted of selective area grown nanowires with a pitch of 1 μm and core diameter of 153 nm. At t = 1530 s (blue line) shell growth starts and the absorption resonance from the HE_{11} mode is only partly visible at 800 nm. At t = 2130 s (red line) the nanowire diameter has increased and the reflectance minima at 572 nm corresponds to a nanowire diameter of 232 nm (absorption from HE_{12} mode). At t = 2730 s (green line) the growth stops and the reflectance minima is found at 659 nm corresponding to a nanowire diameter of 289 nm (absorption from HE_{12} mode) which matches well with the SEM measured value of 285±11nm.

3.3 Doping of Semiconductor Nanowires

Doping is one of the most important properties of a semiconductor since it to a large extent determines the semiconductor's conductivity. It is also necessary in order to make devices such as solar cells and light-emitting diodes which incorporate *p-n* junctions. The extent of, and electrical fields within, a *p-n* junction are largely controlled by the doping levels on the *n-* and *p*-type sides. Control of the doping level is thus essential and one therefore needs to understand how dopants can be incorporated in the crystal.

Doping of nanowire can be accomplished by both ex situ [135] and in situ methods. If the nanowires are grown by a bottom-up technique in situ doping is the most common way to control the doping level [136]. During nanowire growth dopant incorporation can follow two main pathways:

1. Incorporation directly on a surface at a vapour-solid interface.

2. Incorporation through a seed particle i.e. at the liquid-solid or vapour-liquid-solid interfaces

The first pathway is similar to growth of planar layers and occurs in shell growth of particle assisted nanowires. In addition doping through the top and side facets during selective area epitaxy will also follow this pathway. If axial and radial growth occurs simultaneously for selective area nanowires it is expected that dopant incorporation will be different in the axial and radial growth since the dopants will incorporate on different crystal facets [137].

The second pathway is necessary for controlling the doping level in particle assisted nanowires. This pathway also poses the largest difference compared to planar growth since it involves the liquid seed particle. For particle assisted nanowires several reports exist where dopant incorporation on the nanowires side facets has been found to be more efficient than through the particle [138, 139].

The following sections will first give a few examples of how the doping level in nanowires can be measured and quantified. After this, the effect of doping on the morphology of core-shell InP nanowires is discussed where spatially resolved measurements of the carrier concentration proved to be important.

3.3.1 Measuring the Doping Level of Nanowires

Evaluation of doping levels in nanowires is critical for optimising device performance. Many techniques have been reported to give a measure of the doping level including: field-effect transistor (FET) measurements [140], Hall effect measurements [141] (Paper V), C-V profiling [142], Raman spectroscopy [143], electroluminescence

(Paper VI), photoluminescence (PL) [72](Paper VI) and atom probe tomography [138]. A few of the most common techniques along with the techniques used in this thesis are outlined below.

By breaking off single nanowires and using them as a channel in a FET the carrier concentration can be estimated. The carrier concentration is extracted from the resistivity of the nanowire channel by estimating the mobility through the transconductance. However, to extract the mobility, approximations such as describing the nanowire as an infinitely long metallic cylinder and neglecting the capacitive coupling between gate and source-drain contacts are common [144]. Even though these approximations are made, FET measurements are useful for investigating the carrier type and magnitude since the device fabrication and measurements are relatively straightforward and fast.

One of the most common ways to measure the carrier concentration in bulk semiconductors is through Hall effect measurements. Here a magnetic field is applied perpendicular to a current which is driven through the semiconductor. Due to the Lorentz force the carriers in the semiconductor are deflected giving rise to a Hall voltage, which depends on the carrier concentration and carrier type. Fabricating nanowire devices for measuring the Hall effect are challenging due to the extreme accuracy needed for positioning of contacts to measure the Hall voltage [141] (Paper V). Analysis of the measurement data is also not as straightforward as in a bulk sample. To extract the carrier concentration finite element simulations can be used which takes the positioning of the Hall contacts, relative to the nanowire, into account. By placing several Hall voltage probes along the length of a nanowire it is possible to spatially resolve variations in the carrier concentration (Papers V - VII). Spatial resolution of the nanowire doping profile is critical in order to optimize growth conditions for device structures.

Optical measurements provide a convenient way of analysing carrier concentrations in semiconductors (see Figure 3.9) since it does not require processing to form electrical contacts. Starting with an intrinsic semiconductor the luminescence peak position and width is determined by the materials intrinsic bandgap and the temperature. As a small amount of dopants are introduced the luminescence peak redshifts since optical transitions now can occur through the dopant energy level. An even higher amount of doping causes the Fermi level to shift into the conduction band (for *n*-type doping) which results in a blue shift and significant broadening of the luminescence.
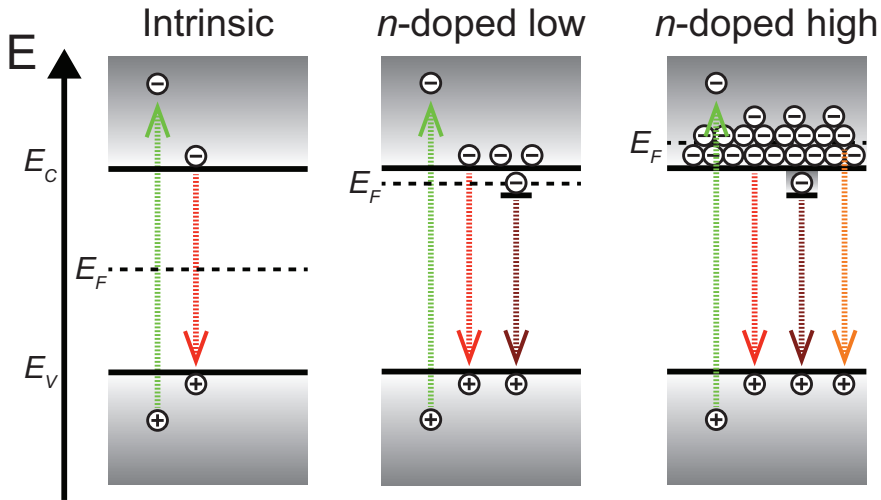
Figure 3.9 Schematic of the recombination processes during a PL experiment in an intrinsic, low *n*-doped and high *n*-doped semiconductor. Green light is used to excite electrons from the valence band (E_V) to the conduction band (E_C) in the semicondcor. Depending on which states the electrons occupy recombination can occur from the conduction band edge, dopant level or within the conduction band. The spectral shape and peak energy of the luminescence changes depending on which recombination processes that occur and can be used to quantify the amount of carriers.

To quantify the amount of doping from a given PL spectra it is possible to consider the luminescence peak position, peak width or the Fermi level tail. For nanowires we have shown that the carrier concentration measured by PL can be correlated to Hall effect measurements within a factor of 2 (Paper VI).

3.3.2 Influence of Doping on Nanowire Shell Growth

In situ doping has been reported to change the shell orientation [145] and morphology [146] of core-shell nanowires. The effects of dopants on the growth have been attributed to changes in the relative growth rates between different facets and changes in the diffusion length of different adatoms as the dopant is introduced.

In Paper VII ZB InP core nanowires doped with Zn were used to study the growth of *n*-type InP shells doped with Sn. The core nanowire structure consisted of a twinning super lattice which exhibits {111} microfacets [71]. During growth of a low doped *n*-type shell the resulting structure consisted of a hexagonal pillar bound by six {1$\bar{1}$0} facets (see Figure 3.10) as expected for ZB InP nanowires grown at a high temperature [147].

As the amount of TESn is increased {111} facets reappears and Sn thus promotes the formation of {111} facets over {1$\bar{1}$0} facets, most likely through formation of a surface

accumulation layer [148]. Sn does however not seem to be the only adatom which affects the formation of {111} vs. {1$\bar{1}$0} facets since at a medium dopant molarfraction of χ_{TESn} = 5*10^{-7} both facets are present at the same time even though the carrier concentration throughout the nanowire shell is constant (Paper VII). The constant carrier concentration suggests a constant In/Sn ratio along the nanowire length. Instead we argue that the surface concentration of phosphorous exhibits a gradient along the length of the nanowire. Phosphorous has been reported to change the growth rate between <111> and <1$\bar{1}$0> directions where a low phosphorous pressure promotes growth on {111} planes and inhibits growth on {1$\bar{1}$0} planes [147]. The gradient of phosphorous and its effect on the nanowire shell facets is further supported by that an increase in χ_{PH3} results in the formation of {1$\bar{1}$0} facets at the top 300 nm of the nanowires, indicating a high amount of phosphorous here (Paper VII).
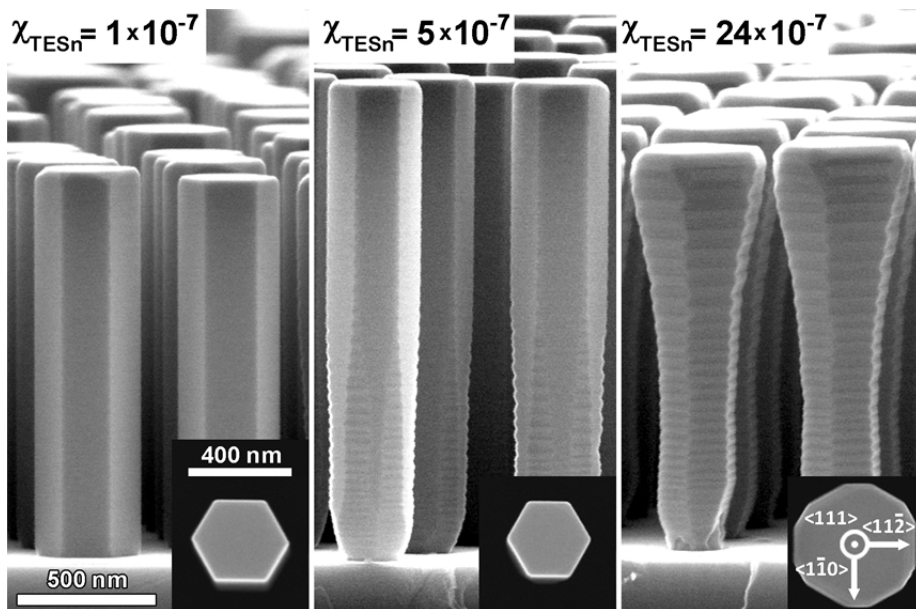

Figure 3.10 Side and top view of three core-shell InP nanowire samples where the shell has been grown with different molarfractions of TESn (χ_{TESn}). A low value of χ_{TESn} promotes {1$\bar{1}$0} side facets while higher flows promote formation of {111} facets. At a medium flow both types of facets can be observed.

4 III-V Nanowire Solar Cells

Nanowires have a potential to reduce the material use and thus also the fabrication cost of solar cells. This can be accomplished through utilizing nanophotonic effects which enhances the light absorption beyond that possible when only considering geometrical optics. There are two different large-area nanowire solar cell designs being considered for future applications (see Figure 4.1). The axial nanowire solar cell design is analogous to the planar solar cell where the light propagation and charge separation occurs in the same direction. The radial nanowire solar cell design takes advantage of the new possibilities that the nanowire geometry offers. Here the charge separation instead occurs orthogonal to the direction of light propagation.

In this chapter the basics of solar cell physics is first introduced and after this the axial and radial solar cell designs are discussed.
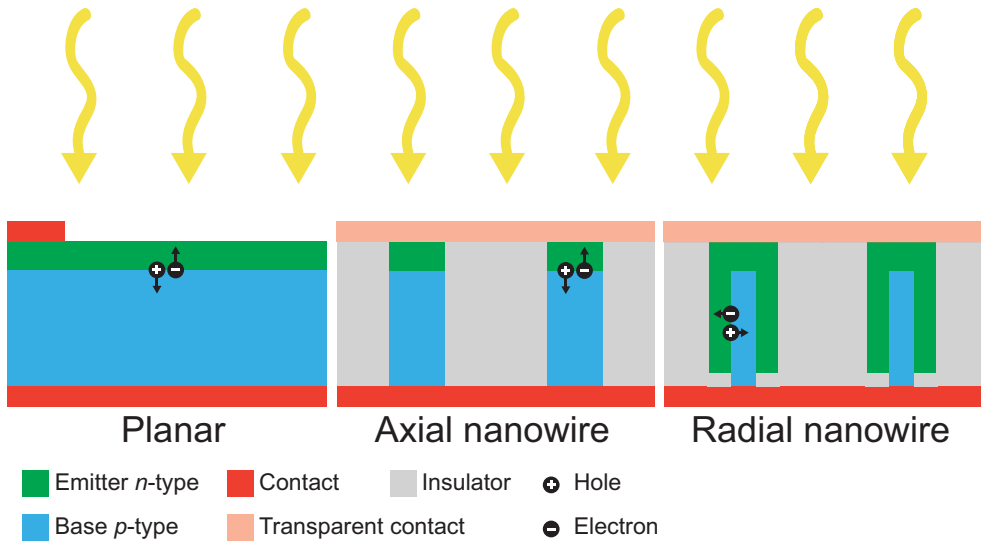

Figure 4.1 Principal structure of a conventional planar, axial nanowire and radial nanowire solar cell. An axial nanowire solar cell is analogous to a planar since charge separation and light propagation occurs in the same direction. In a radial nanowire solar cell charge separation instead occurs orthogonal to the direction of light propagation.

4.1 Solar Cell Physics

A photovoltaic device absorbs the energy of impinging photons and converts it into an output voltage (V) and current density (J). By connecting a load (or resistance) to the photovoltaic device it is possible to extract the power density $P = JV$ [2] which can be used for running appliances, electrical motors etc...

Sunlight is the most abundant source of photons and its spectrum of wavelengths ranges from a few hundred nanometres to a couple of micrometres at the earth's surface (see Figure 4.2). Equivalently, the energy of the photons thus varies from around 4 eV to a few hundred meV. Assuming an average photon energy of 1 eV and the power density of sunlight to be 1000 W/m^2, about 10^{22} photons hits a 1 m^2 surface each second. An efficient solar cell should be able to harvest as much of the energy from these photons as possible.
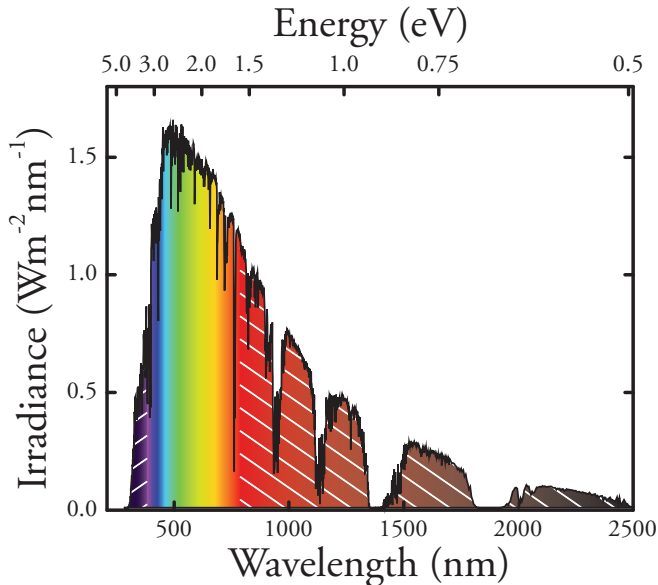
Figure 4.2 AM1.5G reference spectra of sunlight [149] showing the ultraviolet, visible and infrared parts. Light below 300 nm is effectivly absorbed in the atmosphere by oxygen, ozone and nitrogen while dips at longer wavelengths are mainly due to absorption by H_2O and CO_2. The total, un-concentrated, power density is 1000 W/m^2 and is often refered to as 1 sun.

---

[2] The photocurrent is here defined as positive when calculating P, which is the convention within the solar cell community. In the papers included in this thesis this quantity is however defined as negative to follow the convention of current flow of a diode measured in the dark commonly used in semiconductor physics.

A photon which is absorbed by a solar cell excites an electron from a low energy state to a high energy state. In a semiconductor excitation occurs from the valence band to the conduction band. The voltage output of a solar cell depends on the separation between the low and high energy states and will for a semiconductor thus be dependent on its bandgap (E_g). In an ideal picture a larger E_g thus results in a larger output voltage [150]. Absorption in the solar cell, which leads to excitation of electrons that can contribute to J, can however only occur at photon energies above E_g and thus a larger E_g results in a smaller J. Electrons that are excited by photons carrying more energy than E_g will lose the excess energy due to thermalisation. The output J and V thus show the opposite dependence on E_g where V tends to increase with increasing E_g and J tends to decrease with increasing E_g. It turns out that the optimal E_g of a solar cell lies between 1.0 and 1.6 eV [151]. The theoretical maximum efficiency for a terrestrial solar cell at 1 sun is 31% and is reached when E_g = 1.35 eV [152].

4.1.1 The *p-n* Junction as a Solar Cell

To extract a current from a solar cell, it is necessary to form two contacts to the absorbing material. These contacts should be selective so that one contact only extracts electrons from the conduction band and the other contact only extracts holes from the valence band. In high efficiency solar cells this is accomplished by the formation of a *p-n* junction. Space charges at the interface between the *p-* and *n*-sides create a built-in electric field which drives a drift current of the photogenerated carriers. Electrons will then travel towards the *n*-side while holes travel towards the *p*-side (see Figure 4.3).

If the contacts to the *p-* and *n*-side are put at equal potential, i.e., short circuited, the current density of the solar cell is maximum and defined as the short circuit current density J_{SC}. This property is determined by the incident photon flux density and the solar cells quantum efficiency (QE). QE is in turn dependent on the absorption and charge separation efficiency of the solar cell [153].

As a load is added to the external circuit a potential builds up between the two contacts caused by a separation of the quasi Fermi levels (E_{Fp} and E_{Fn}) on the *p-* and *n*-sides. The current density through the device is now determined by the superposition of J_{SC} and the diode equation which results in:

$$J = J_{SC} - J_0(e^{qV/kT} - 1). \tag{4.1}$$

In Eq. (4.1) J_0 is the reverse saturation current density, q is the electron charge, k is Boltzmann's constant and T is the temperature.

By increasing the voltage across the *p-n* junction the diffusion current density, described by the ideal diode equation, increases. When the magnitude of the diffusion

current density equals that of J_{SC} the net current through the device is zero. At this point the voltage across the solar cell is maximised and termed the open-circuit voltage (V_{OC}). From Eq. (4.1) it is possible to extract an expression for the V_{OC} by setting $J = 0$ and realising that $e^{qV/kT} \gg 1$:

$$V_{OC} = \frac{kT}{q} \ln\left(\frac{J_{SC}}{J_0}\right). \tag{4.2}$$

From Eq. (4.2) we find that the V_{OC} will depend on the incident photon flux and the QE through J_{SC}, the reverse saturation current J_0 and the temperature. By increasing J_{SC} through concentration it is possible to boost the V_{OC}. The boost in V_{OC} in turn increases the efficiency and the highest reported single band gap solar cell conversion efficiency to date (29.1%) was measured at a concentration corresponding to 117 suns [154].
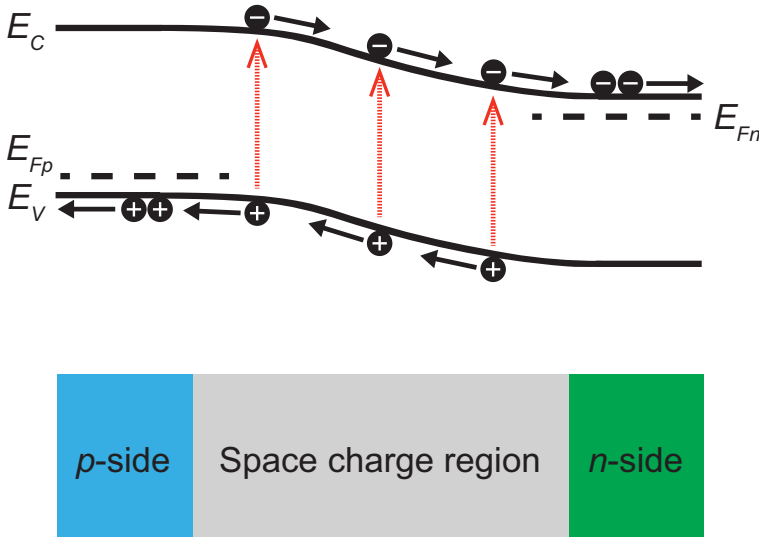
Figure 4.3 Schematic of a *p-n* junction working as a solar cell. Absorption of light creates electron-hole pairs which are separated in the space charge region giving rise to a drift current.

Besides from the obvious temperature dependence in Eq. (4.2) J_0 also has a strong dependence on temperature. The diffusive component of J_0 can be expressed as [155]:

$$J_0 = J_{00}n_i^2 = J_{00}N_C N_V e^{-E_g/kT}. \tag{4.3}$$

Here J_{00} depends on the diffusion length of the minority carriers on either side of the *p-n* junction, n_i is the intrinsic carrier concentration and N_C and N_V are the effective density of states in the conduction and valence bands. Combining Eq. (4.2) and (4.3) we can find a temperature expression for the V_{OC}:

$$V_{OC} = \frac{kT}{q} \ln\left(\frac{J_{SC}}{J_{00}N_C N_V} e^{E_g/kT}\right) = \frac{E_g}{q} + \frac{kT}{q} \ln\left(\frac{J_{SC}}{J_{00}N_C N_V}\right) =$$

$$= \frac{E_g}{q} - \frac{kT}{q} \ln\left(\frac{J_{00}N_C N_V}{J_{SC}}\right). \tag{4.4}$$

The last step in Eq. (4.4) is made to emphasize that $J_{SC} < J_{00}N_C N_V$ and the V_{OC} thus decreases with increasing temperature. Additional temperature dependences within J_{00}, N_C and N_V also exists but can be considered small compared to the exponential dependence of n_i [156]. Eq. (4.4) shows that E_g can be extracted from a temperature dependent measurement of the V_{OC} by extrapolating to T = 0 K.

4.1.2 Performance Metrics of a Solar Cell

Regardless of how a solar cell is fabricated its performance is characterised by a few key figures. Most important is of course the efficiency (η) which is defined as the ratio between the maximum power density (P_{Max}) produced by the solar cell and the incident light power density (P_{Light}). The maximum power density of the solar cell is reached when the product of J and V along the solar cells J-V curve is maximum which occurs at the maximum power point (J_{MP}, V_{MP}) (see Figure 4.4). The ratio between P_{Max} and the power density obtained as the product of J_{SC} and V_{OC} is the fill factor (FF). This can be visualised as the ratio between the two blue rectangles in Figure 4.4. Using these terms one can define the efficiency as:

$$\eta = \frac{P_{Max}}{P_{Light}} = \frac{J_{MP}V_{MP}}{P_{Light}} = \frac{J_{SC}V_{OC}FF}{P_{Light}}. \tag{4.5}$$

As discussed in the previous section J_{SC} depends on the QE of the solar cell which is related to the absorption and charge separation efficiency. V_{OC} depends on several factors such as light concentration, temperature and J_0. Both the light concentration and temperature can be optimised on a system level but J_0 is an intrinsic property which must be optimised in the solar cell material fabrication. J_0 originates from recombination in the solar cell which should be reduced in order to not degrade the V_{OC}. The FF can be reduced if there is a large series resistance or a low shunt resistance in the solar cell device.
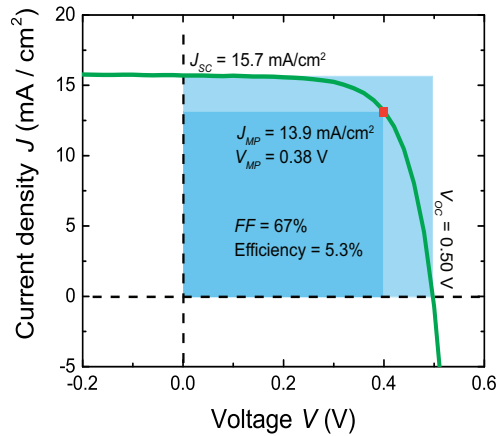
Figure 4.4 *J-V* curve of a nanowire array solar cell from Paper VIII where the *p-n* junction was defined in the radial direction. Key performance figures are marked such as the efficiency, *FF*, maximum power point, J_{SC} and V_{OC}. The incident light consisted of the AM1.5G spectra and had a power density of 1000 W/m², equivalent to 1 sun.

4.1.3 Multi-junction solar cells

Several strategies have been proposed to increase the efficiency of semiconductor solar cells. For an ideal solar cell two main loss mechanisms exist. First, photons with energy smaller than the bandgap are not absorbed and can thus not contribute to the photocurrent. Second, photons with energy higher than the bandgap quickly loose the excess energy due to thermalisation as the carriers relax to states close to the band edges. Both these effects are linked by how the bandgap of the solar cell is chosen. A small bandgap gives more thermalisation losses while a high bandgap gives more absorption losses.

The most successful way of overcoming these fundamental losses has been the realisation of solar cells which contain several sub-cells with different bandgap. Each sub-cell can then absorb a selected part of the solar spectrum resulting in reduced thermalisation and absorption losses. The most prevalent way to fabricate these cells has been the monolithic integration of sub-cells stacked on top of each other [157]. The top cell consists of a high bandgap material, which subsequently lets photons with energy below its bandgap pass through. These low energy photons are absorbed by the low bandgap cell underneath (see Figure 4.5). The different sub-cells, which each contain their own *p-n* junction, are connected through a highly doped reverse biased junction called a tunnel junction. On either side of the *p-n* junctions in the sub-cells are passivation layers of a high bandgap material to prevent losses due to recombination at the surface and interfaces to highly doped material [158].
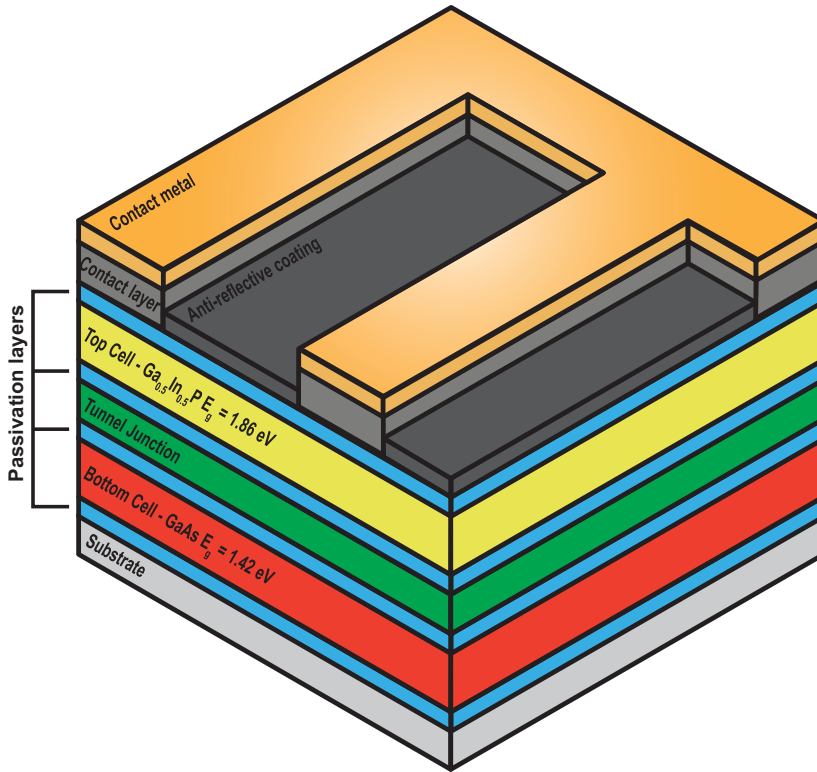
Figure 4.5 Schematic of a tandem solar cell with monolithically integrated sub-cells. Cell structure adapted from ref. [158].

At a concentration of 1000 suns the ultimate efficiency is increased from 37% of a 1-junction solar cell to 50, 56 and 72% of a 2-, 3- and 36-junction solar cell [152]. The efficiency record for an epitaxially integrated cell structure is currently 45.7% using 4-junctions at a concentration of 234 suns [154].

Adding more junctions increases the complexity of the structure since present technology relies on epitaxial growth of planar layers. Because the layers are stacked on top of each other, the choice of materials (or equivalently bandgaps) is limited by lattice matching constraints. In the highest efficiency 3- and 4- junction solar cells this has been partly circumvented by implementation of metamorphic buffer layers which gradually reduce the strain between lattice mismatched sub-cells [159]. Without such a buffer layer the sub-cells would be filled with defects drastically reducing their performance. An alternative approach to epitaxial growth of a monolithically integrated cell is separate growths of the different junctions, and later the final solar cell is assembled through wafer bonding [160]. With this approach it is possible to choose bandgap combinations more freely while maintaining a high material quality, at the expense of adding additional MOVPE and processing steps.

4.2 Axial Nanowire Solar Cells

Axial nanowire solar cells are analogous to planar solar cells in the sense that the charge separation occurs in the same direction as the light propagates. This nanowire geometry has so far produced the highest efficiency nanowire solar cells with a record of 15.3% for a bottom-up fabricated nanowire structure [91]. Axial solar cells have a distinct advantage over planar and radial nanowire solar cells in its small junction area. Looking at Eq. (4.2) we find that the V_{OC} depends logarithmically on the ratio J_{SC}/J_0. Assuming that material parameters that govern J_0 are the same, the smaller junction area of the axial solar cell leads to an increase of J_{SC}/J_0, since J_0 will depend on the junction area [161]. This will have a similar effect as concentration and lead to an increase in the V_{OC}. This effect is a probable explanation for the high V_{OC} reported for the axial nanowire solar cells, which can exceeded that of record planar solar cells [10].

The increased knowledge of absorption, charge separation and surface passivation in nanowire solar cells over the past five years have established a few guiding principles in nanowire solar cell design. Below, a few of the most important aspects taking modelling and experimental results into account are listed:

- *Nanowire array geometry:* As was already discussed in section 3.2, the reflection and absorption of a nanowire array depends on the nanowire length, diameter and pitch. These three parameters must be optimized in order to achieve as high absorption of light as possible. Simulations suggest that optimal diameters for absorption can be found when wavelengths close to the bandgap are strongly coupled into the nanowires. For InP, diameters around 180 and 400 nm are suitable since there the HE_{11} and HE_{12} modes, discussed in section 3.2.2, are excited at energies close to E_g. For more broadband absorption dual-diameter nanowires could also be considered [162]. The nanowire length and pitch show a strong dependence on each other. For short nanowires the pitch should be small in order to enhance absorption while for long nanowires the pitch should be large. A large pitch decreases reflection losses at the top of the nanowire array and thus increases the absorption [134, 163].

- *Junction design:* A planar solar cell is usually designed with a thick low doped base and a thin highly doped emitter [164]. As light impinges on the cell it first reaches the emitter where high energy photons are absorbed. The generated minority carriers have a large chance of recombination either at the contact or because of the high doping level which reduces J_{SC}. The same trend has been observed in nanowires where a short junction depth, on the order of 100 nm, is desired for high efficiencies [10, 92].

- *Surface passivation:* In situ surface passivation has so far not been necessary to achieve efficiencies above 10% for InP nanowire solar cells [10]. This is probably due to the fact that InP has a low surface recombination velocity. In addition, a layer of

SiO$_2$ is often used to insulate the nanowire sidewalls from the top contact. This can increase the carrier lifetime and thus also act as a surface passivation [165]. For GaAs the surface recombination velocity is higher and steps must be taken to reduce it. This can be done with in situ surface passivation such as AlGaAs [91], or by increasing the nanowire diameter and thus reducing the surface-to-volume ratio [92].

4.2.1 Towards Multi–Junction Nanowire Solar Cells

There are two principle types of designs to consider when forming a multi-junction solar cell incorporating nanowires. The first design consists of a planar junction in the substrate, for example Si, and on top a second junction (or more) in a nanowire with suitable bandgap. Between the two junctions, a tunnel junction would be used to establish electrical connection, similar as a planar tandem cell (see Figure 4.5). Since it is possible to grow lattice mismatched nanowires on top of a Si substrate there is a distinct advantage over planar technology, which usually uses Ge or GaAs substrates. The optimum bandgap of the nanowire top junction in a tandem configuration is around 1.7 eV, when the bottom cell consists of Si. Simulations suggests that this could give efficiencies above 30% at 1 sun concentration [166].

In the second design the junctions would be entirely within the nanowires which would give the possibility to freely choose suitable bandgaps for each sub-cell. Since the substrate only acts as an epitaxial support during fabrication it can be removed afterwards in a peel-off process [167](Paper XIV). For this geometry optimal bandgaps would be 0.94-1.60 eV, 0.94-1.37-1.90 eV and 0.71-1.11-1.49-2.00 eV for a two-, three- or four-junction solar cell. The theoretical maximum efficiency is around 55% for a planar four-junction cell [168].

To produce a multi-junction nanowire solar cell *p-n* junctions in materials with suitable bandgap are required along with tunnel diodes to connect the different sub-cells. *p-n* junctions from alloys such as InGaAs [58] and GaInP [169] which can be tuned to the desired bandgap combinations have been shown. Additionally, tunnel junctions at the Si-nanowire interface [170] and along the axial direction of the nanowire [171, 172] have been successfully made.

Connecting two *p-n* junctions in series using a tunnel diode has so far only been shown in single bandgap structures [173](Paper II). In paper II, two InP *p-n* junctions were connected in series through an InP tunnel junction. The structure was grown on a Si substrate and is outlined in Figure 4.6a. Electrical measurements under illumination showed an increase in the V_{OC} for the tandem junction compared to a single InP junction (see Figure 4.6b). The increase in V_{OC} is a clear sign of voltage addition between the two junctions even though the total voltage was below E_g/q for InP. A temperature dependent measurement however gives more clear evidence if the two junctions were connected properly (see Eq. (4.4)). An extrapolated value of $V_{OC} = 2.49$ V at T = 0 K was obtained which is clearly above E_g/q for InP.
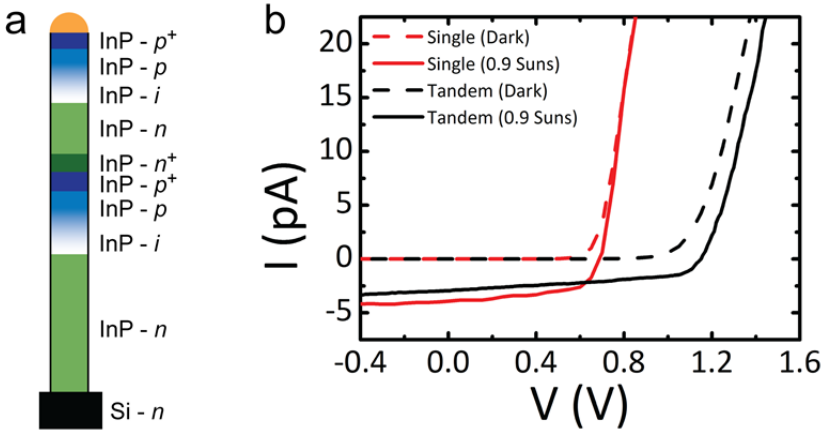
Figure 4.6 (a) Schematic of the InP tandem structure used in Paper II. Doping is indicated by the different colors green (*n*-type), blue (*p*-type) and white (intrinsic). A darker color indicates higher doping. **(b)** Electrical measurements on single nanowires broken off from the growth substrate, with a single or tandem junction. Measurements were performed in the dark and under 0.9 suns where a photocurrent could be measured.

4.3 Radial Nanowire Solar Cells

By placing the *p-n* junction in the radial direction, charge separation and light propagation become decoupled. This is especially beneficial if the diffusion length of minority carriers is short compared to the cell thickness, since then J_{SC} will increase [174]. However, at the same time the increased junction area will, as was discussed in section 4.2, tend to increase J_0. If the ratio J_{SC}/J_0 decreases, the V_{OC} will consequently drop according to Eq. (4.2).

To date, the highest achieved efficiency of a bottom-up fabricated III-V radial nanowire solar cell is 7.4% [57]. To achieve high efficiencies a few common design features have been found which are listed below:

- *Nanowire array geometry:* In terms of nanowire diameter and pitch, the requirement is the same as for axial nanowire solar cells discussed in section 4.2, since absorption should be maximized. The nanowire length will have an effect on both J_{SC} and the V_{OC}. For short nanowires, absorption will be insufficient resulting in a low J_{SC}. Conversely if the nanowire length is longer than necessary for effective absorption the V_{OC} will decrease due to the increase in J_0, which accompanies the increased junction area [161, 174]. A balance must thus be found where the nanowires are long enough so photons are efficiently absorbed, at the same time as J_0 is not increased too much.

- *Junction design:* The built in voltage, and thus the V_{OC} depends on the doping level of the core and shell, the core diameter and the shell thickness. Since the thickness of the emitter (shell) and base (core) in a radial solar cell is small compared to a planar solar cell, there is a risk of fully depleting either the shell, the core or both. To avoid this, the doping levels in the core and shell should be relatively high to decrease the width of the depletion region in the *p-n* junction [175]. Also here a shallow junction could be beneficial. In a top-down fabricated nanowire solar cell a shallow one-sided junction, formed by ex situ doping, has shown a high efficiency of above 8% [135].

- *Surface passivation:* The two bottom-up radial nanowire solar cell designs with highest efficiency (7.4% and 6.4%) have both employed in situ surface passivation [57, 176]. In both cases, substantial increases were observed in both J_{SC} and V_{OC} compared to unpassivated junctions. The increase in J_{SC} was attributed to reduced recombination of photogenerated carriers in the shell. For the surface passivation to be effective it should provide a barrier for the minority carriers in the emitter. For InP the choice has so far been $Al_{0.05}In_{0.95}P$, even though it is lattice mismatched, since it provides a relatively large band offset in the valence band, and is thus suitable for an *n*-type emitter. For GaAs several lattice matched alternatives exist such as $Ga_{0.5}In_{0.5}P$, $Al_xGa_{1-x}As$ and $Al_{0.5}In_{0.5}P$. Another approach to increase extraction of carriers generated close to the contact is to form the junction at the interface between the contact and nanowire [177].

4.3.1 Strategies for Higher Efficiency

The main drawback of radial nanowire solar cells so far has been low values of the V_{OC}. Both for InP and GaAs, record efficiency radial nanowire cells have a V_{OC} in the region of 0.5 - 0.6 V [57, 176] even though their axial nanowire counterparts have shown a V_{OC} in the region 0.8 - 0.9 V [10, 91]. Simulations have shown that the V_{OC}, besides being sensitive to surface states, also is sensitive to trap assisted (Shockley-Read-Hall) recombination [161]. This type of recombination is especially strong in the space charge region where electron and hole concentrations are similar [178]. It is therefore important to limit the amount of recombination centres at the core-shell interface which often resides in the middle of the depletion region.

Both the reverse saturation current and trap assisted recombination will depend on the *p-n* junction area. In Paper VIII a growth method was developed which is able to reduce the junction area of a radial *p-n* junction while keeping the nanowire length sufficiently long for high absorption. A schematic of the growth process is outlined in Figure 4.7 along with a SEM image of the final device structure. Due to the smaller junction area the device showed a high V_{OC} exceeding that of a surface passivated InP radial nanowire solar cell [176]. Adding a capping layer should lead to additional increases in both V_{OC} and J_{SC}.

The growth method in Paper VIII also facilitated a comparison between single nanowire measurements and measurements on solar cell devices fabricated from nanowire arrays. This showed that using the geometrical area of a single nanowire to estimate the efficiency, of a horizontal single nanowire device, gives an error of approximately a factor of 2 (Paper VIII). Since the nanowires are smaller than the wavelengths that they absorb, the absorption cross-section can be larger than the geometrical area of the nanowire. This shows that in order to give relevant values of nanowire solar cell efficiencies nanowire arrays should be used.

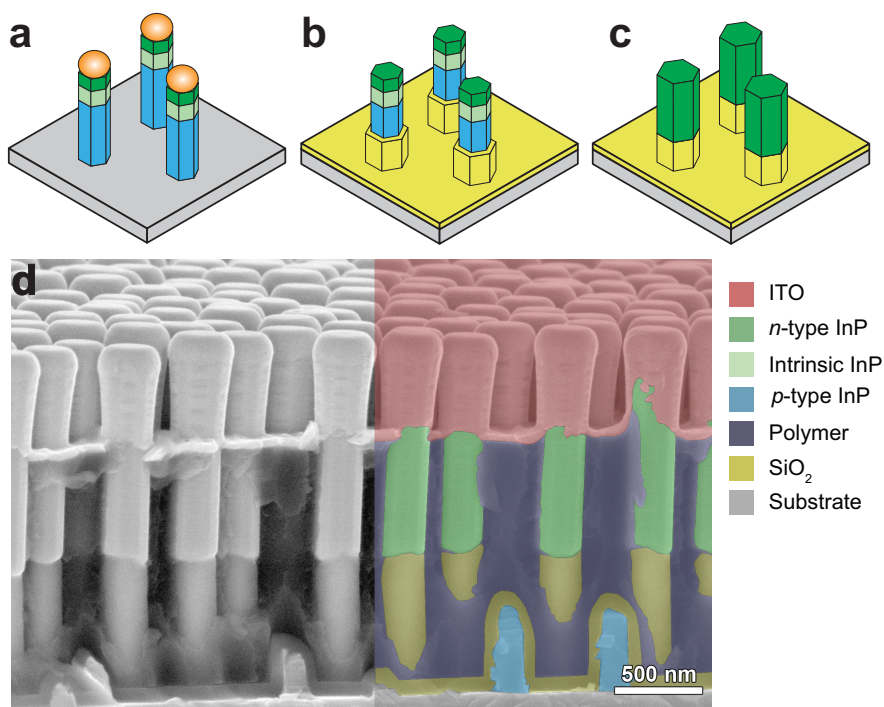**Figure 4.7 (a)-(c)** Schematic of the growth process used in Paper VIII. **(a)** Particle assisted core nanowire growth of a *p-i-n* structure. **(b)** The Au particle is removed in a wet etch process and SiO₂ is deposited by ALD which is subsequently etched back. **(c)** Regrowth of an *i-n* shell where the SiO₂ now masks part of the core. **(d)** Partially false colored cross section SEM image of a contacted device.

5 Summary and Outlook

The results obtained in this thesis show that it is possible to fabricate semiconductor nanowires of high quality over large areas. This can be accomplished by growing the nanowires on a substrate in a regular pattern defined by nanoimprint lithography, or by producing a large amount of nanowires in the continuous Aerotaxy process.

For substrate grown nanowires the particle assisted and selective area growth techniques can be used. With both techniques it is possible to reproducibly grow nanowire arrays with very small spread in diameter and length. This makes them suitable for use in opto-electronic devices where nanophotonic effects such as resonant absorption can be utilised. By using in situ measurements the entire growth process can be monitored. This can be used to reveal the complex dynamics of nanowire growth where one needs to take factors such as precursor decomposition and surface diffusion into account. This complex dynamics was observed to affect the incorporation of dopants during shell growth. Here gradients of different growth species along the nanowire length were found which had an impact on the nature of the nanowire side facets. Additionally, it also caused a gradient in the carrier concentration along the nanowire length at high doping levels.

Aerotaxy grown nanowires show a large potential if nanowires should be incorporated in very large area devices. This advantage mainly originates from lower fabrication costs as the growth process does not use any substrate and is continuous. In order for the technique to be successful it will be important to show that it is flexible enough to fabricate structures incorporating several layers which are suitable for devices. Equally important is to develop a process which can align billions of nanowires so they can be contacted in a vertical orientation over a large area.

The future is bright for incorporating nanowires into solar cells where only a fraction of the active material will be required compared to current planar solar cells. For this purpose two different device geometries have been discussed where the *p-n* junction is formed in the axial or radial direction. Through continued development towards multi-junction nanowire solar cells efficient use of the solar spectrum is possible.

In order for nanowire solar cells to take the next step, and become an alternative in future solar cells, several factors will be important. First of all efficiency must be improved further. The first target should be to exceed the 20% efficiency mark and thus have record efficiencies comparable to other thin-film technologies such as CIGS and CdTe. This should be possible to reach by optimising light absorption further,

reducing recombination losses and improving contacting schemes. After this there are two possible routes which both involve the formation of a multi-junction structure.

The first route involves the monolithic integration of several junctions in the actual nanowire structure. The different sub-cells should then be connected through tunnel junctions. This technology combined with the possibility of reusing the substrate can result in high efficiency solar cells which use a small amount of material. Since multi-junction structures are fairly complex (an efficient tandem structure involves at least 10 different layers) MOVPE will be the most suitable technique for the nanowire growth. An interesting question will of course be how many sub-cells that will be required to reach efficiencies which make the nanowire technology competitive.

The second route is based on fabricating a single junction nanowire solar cell with a bandgap which is complementary to Si in a tandem junction structure. The nanowire solar cell can then be integrated with today's dominant commercial PV technology, boosting its efficiency. The advantage of this route is a less complex design of the nanowire solar cell and that the Si planar solar cell technology is well developed. With a simpler design of the nanowire structure it would be possible to use a low cost growth method such as Aerotaxy to grow the nanowires.

In order to reach the goals set out by for example the European Union, where greenhouse emissions should be reduced by more than 80% until 2050, electricity production from solar cells must increase substantially. Currently electricity from PV installations account for 3% of the electricity production in Europe. Considering a future energy mix of mainly solar, wind, and hydro perhaps solar cells will account for 30-50% of the European electricity production. Although this seems challenging, growth of PV installations by a factor of 10 is highly realistic. Between 2008 and 2013 we saw a similar growth from 7 TWh to 80 TWh of electricity produced by solar cells in Europe. Continued innovation and a more mature PV market will make solar cells the most cost effective renewable energy source in many places in Europe and the world as a whole.

If nanowires will be part of the solution for future electricity production it is good to already now get a sense for the scale needed in the nanowire production process. Worldwide PV production is expected to reach 200 GW on an annual basis sometime after 2025. If nanowire solar cells obtain a 5% market share by this time we would have to produce 50 million square metres of nanowire solar panels each year (assuming a module efficiency of 20%). On each square metre of solar panel the active nanowire layer would weigh just above 1 g equating to a total yearly nanowire production of above 50 tonnes. This would require us to grow, position and contact on the order of 10^{20} nanowires each year.

References

1. IEA, *Key World Energy Statistics*, 2014

2. IPCC, *Climate Change 2014: Synthesis Report. Contribution of Working Groups I, II and III to the Fifth Assessment Report of the Intergovernmental Panel on Climate Change*, 2014 p. 9.

3. Crabtree, G.W. and Lewis, N.S., *Solar energy conversion,* Physics Today **60** (2007) p. 37-42.

4. EPIA, *Global Market Outlook for Photovoltaics 2014-2018*,

5. IEA PVPS, *Snapshot of Global PV Markets 2014*, 2015

6. IEA, *Technology Roadmap - Solar Photovoltaic Energy*, 2014

7. First Solar press release, *FIRST SOLAR PASSES $1 PER WATT INDUSTRY MILESTONE*, 24th February 2009.

8. Kost, C. et al., *Levelized Cost of Electricity - Renewable Energy Technologies*, 2013

9. de Wild-Scholten, M.J., *Energy payback time and carbon footprint of commercial photovoltaic systems,* Solar Energy Materials and Solar Cells **119** (2013) p. 296-305.

10. Wallentin, J. et al., *InP Nanowire Array Solar Cells Achieving 13.8% Efficiency by Exceeding the Ray Optics Limit,* Science **339** (2013) p. 1057-1060.

11. Ford, A.C. et al., *Diameter-Dependent Electron Mobility of InAs Nanowires,* Nano Letters **9** (2009) p. 360-365.

12. Björk, M.T. et al., *One-dimensional Steeplechase for Electrons Realized,* Nano Letters **2** (2002) p. 87-89.

13. Gudiksen, M.S. et al., *Growth of nanowire superlattice structures for nanoscale photonics and electronics,* Nature **415** (2002) p. 617-620.

14. Mårtensson, T. et al., *Epitaxial III–V Nanowires on Silicon,* Nano Letters **4** (2004) p. 1987-1990.

15. Morales, A.M. and Lieber, C.M., *A laser ablation method for the synthesis of crystalline semiconductor nanowires,* Science **279** (1998) p. 208-211.

16. Geisz, J.F. et al., *40.8% efficient inverted triple-junction solar cell with two independently metamorphic junctions,* Applied Physics Letters **93** (2008) p. 123505.

17. Isamu, A. and Hiroshi, A., *Crystal Growth and Conductivity Control of Group III Nitride Semiconductors and Their Application to Short Wavelength Light Emitters,* Japanese Journal of Applied Physics **36** (1997) p. 5393.

18. Nakamura, S., Mukai, T., and Senoh, M., *Candela-class high-brightness InGaN/AlGaN double-heterostructure blue-light-emitting diodes,* Applied Physics Letters **64** (1994) p. 1687-1689.

19. Thijs, P.J.A. et al., *High-performance 1.5 μm wavelength InGaAs-InGaAsP strained quantum well lasers and amplifiers,* Quantum Electronics, IEEE Journal of **27** (1991) p. 1426-1439.

20. Kossel, W., *Zur Theorie des Kristallwachstums,* Nachrichten von der Gesellschaft der Wissenschaften zu Göttingen, Mathematisch-Physikalische Klasse (1927) p. 135-143.

21. Smith, D.L., *Thin-film deposition: principles and practice*, McGraw-Hill: New York, 1995, p. 146-147.

22. Giling, L.J. and Van Enckevort, W.J.P., *On the influence of surface reconstruction on crystal growth processes,* Surface Science **161** (1985) p. 567-583.

23. Cui, Y., Wei, Q., Park, H., and Lieber, C.M., *Nanowire Nanosensors for Highly Sensitive and Selective Detection of Biological and Chemical Species,* Science **293** (2001) p. 1289-1292.

24. Sköld, N. et al., *Growth and Optical Properties of Strained GaAs–Ga$_x$In$_{1-x}$P Core–Shell Nanowires,* Nano Letters **5** (2005) p. 1943-1947.

25. Gibbs, J.W., *Collected works*, Longmans, Green and Co.: New York, 1928.

26. Smith, D.L., *Thin-film deposition: principles and practice*, McGraw-Hill: New York, 1995, p. 155.

27. Asai, H., *Anisotropic lateral growth in GaAs MOCVD layers on (001) substrates,* Journal of Crystal Growth **80** (1987) p. 425-433.

28. Stringfellow, G.B., *Organometallic Vapor-Phase Epitaxy: Theory and Practice*, Academic Press: San Diego, 1999, p. 11.

29. Stringfellow, G.B., *Organometallic Vapor-Phase Epitaxy: Theory and Practice*, Academic Press: San Diego, 1999.

30. Borgström, M.T. et al., *In situ etching for total control over axial and radial nanowire growth,* Nano Research **3** (2010) p. 264-270.

31. Thuy, T.T.V. et al., *High optical quality single crystal phase wurtzite and zincblende InP nanowires,* Nanotechnology **24** (2013) p. 115705.

32. Joyce, H.J. et al., *Twin-Free Uniform Epitaxial GaAs Nanowires Grown by a Two-Temperature Process,* Nano Letters **7** (2007) p. 921-926.

33. Borgström, M.T. et al., *Interface study on heterostructured GaP–GaAs nanowires,* Nanotechnology **17** (2006) p. 4010.

34. Caroff, P. et al., *High-Quality InAs/InSb Nanowire Heterostructures Grown by Metal–Organic Vapor-Phase Epitaxy,* Small **4** (2008) p. 878-882.

35. Perea, D.E. et al., *Controlling Heterojunction Abruptness in VLS-Grown Semiconductor Nanowires via in situ Catalyst Alloying,* Nano Letters **11** (2011) p. 3117-3122.

36. Hocevar, M. et al., *Growth and optical properties of axial hybrid III–V/silicon nanowires,* Nature Communications **3** (2012) p. 1266.

37. Haraguchi, K., Katsuyama, T., and Hiruma, K., *Polarization dependence of light emitted from GaAs p-n junctions in quantum wire crystals,* Journal of Applied Physics **75** (1994) p. 4220-4225.

38. Lehmann, S., Jacobsson, D., Deppert, K., and Dick, K., *High crystal quality wurtzite-zinc blende heterostructures in metal-organic vapor phase epitaxy-grown GaAs nanowires,* Nano Research **5** (2012) p. 470-476.

39. Wagner, R.S. and Ellis, W.C., *VAPOR-LIQUID-SOLID MECHANISM OF SINGLE CRYSTAL GROWTH,* Applied Physics Letters **4** (1964) p. 89-90.

40. Barns, R.L. and Ellis, W.C., *Whisker Crystals of Gallium Arsenide and Gallium Phosphide Grown by the Vapor—Liquid—Solid Mechanism,* Journal of Applied Physics **36** (1965) p. 2296-2301.

41. Liu, Z. et al., *Soluble InP and GaP Nanowires: Self-Seeded, Solution–Liquid–Solid Synthesis and Electrical Properties,* Chemistry – A European Journal **15** (2009) p. 4546-4552.

42. Kornienko, N. et al., *Solution Phase Synthesis of Indium Gallium Phosphide Alloy Nanowires,* ACS Nano **9** (2015) p. 3951-3960.

43. Persson, A.I. et al., *Solid-phase diffusion mechanism for GaAs nanowire growth,* Nature Materials **3** (2004) p. 677-681.

44. Borgström, M., Deppert, K., Samuelson, L., and Seifert, W., *Size- and shape-controlled GaAs nano-whiskers grown by MOVPE: a growth study,* Journal of Crystal Growth **260** (2004) p. 18-22.

45. Kodambaka, S., Tersoff, J., Reuter, M.C., and Ross, F.M., *Diameter-Independent Kinetics in the Vapor-Liquid-Solid Growth of Si Nanowires,* Physical Review Letters **96** (2006) p. 096105.

46. Givargizov, E.I., *Fundamental aspects of VLS growth,* Journal of Crystal Growth **31** (1975) p. 20-30.

47. Glas, F., Harmand, J.-C., and Patriarche, G., *Why Does Wurtzite Form in Nanowires of III-V Zinc Blende Semiconductors?,* Physical Review Letters **99** (2007) p. 146101.

48. Wacaser, B.A. et al., *Preferential Interface Nucleation: An Expansion of the VLS Growth Mechanism for Nanowires,* Advanced Materials **21** (2009) p. 153-165.

49. Algra, R.E. et al., *The Role of Surface Energies and Chemical Potential during Nanowire Growth,* Nano Letters **11** (2011) p. 1259-1264.

50. Wen, C.Y. et al., *Periodically Changing Morphology of the Growth Interface in Si, Ge, and GaP Nanowires,* Physical Review Letters **107** (2011) p. 025503.

51. Glas, F., Harmand, J.-C., and Patriarche, G., *Nucleation Antibunching in Catalyst-Assisted Nanowire Growth,* Physical Review Letters **104** (2010) p. 135501.

52. Shaw, D.W., *Selective Epitaxial Deposition of Gallium Arsenide in Holes,* Journal of The Electrochemical Society **113** (1966) p. 904-908.

53. Andrews, D.A., Rejman-Greene, M.A.Z., Wakefield, B., and Davies, G.J., *Selective area growth of InP/InGaAs multiple quantum well laser structures by metalorganic molecular beam epitaxy,* Applied Physics Letters **53** (1988) p. 97-98.

54. Yoo, H.J. et al., *Fabrication of lateral planar InP/GaInAsP heterojunction bipolar transistor by selective area epitaxial growth,* Electronics Letters **25** (1989) p. 191-192.

55. Mohan, P., Motohisa, J., and Fukui, T., *Fabrication of InP/InAs/InP core-multishell heterostructure nanowires by selective area metalorganic vapor phase epitaxy,* Applied Physics Letters **88** (2006) p. 133105.

56. Goto, H. et al., *Growth of Core-Shell InP Nanowires for Photovoltaic Application by Selective-Area Metal Organic Vapor Phase Epitaxy,* Applied Physics Express **2** (2009) p. 035004.

57. Mariani, G., Zhou, Z., Scofield, A., and Huffaker, D.L., *Direct-Bandgap Epitaxial Core– Multishell Nanopillar Photovoltaics Featuring Subwavelength Optical Concentrators,* Nano Letters **13** (2013) p. 1632-1637.

58. Nakai, E. et al., *InGaAs axial-junction nanowire-array solar cells,* Japanese Journal of Applied Physics **54** (2015) p. 015201.

59. Hiruma, K. et al., *Fabrication of Axial and Radial Heterostructures for Semiconductor Nanowires by Using Selective-Area Metal-Organic Vapor-Phase Epitaxy,* Journal of Nanotechnology **2012** (2012) p. 29.

60. Hjort, M. et al., *Surface morphology of Au-free grown nanowires after native oxide removal,* Nanoscale **7** (2015) p. 9998-10004.

61. Duan, X.F. and Lieber, C.M., *General synthesis of compound semiconductor nanowires,* Advanced Materials **12** (2000) p. 298-302.

62. Björk, M.T., *Nanowire Technology for GaAsP/Si Tandem Cells Beyond 25% Efficiency*, Conference talk at EWMOVPE 2015.

63. Hiruma, K. et al., *Growth and optical properties of nanometer-scale GaAs and InAs whiskers,* Journal of Applied Physics **77** (1995) p. 447-462.

64. Thelander, C. et al., *Effects of Crystal Phase Mixing on the Electrical Properties of InAs Nanowires,* Nano Letters **11** (2011) p. 2424-2429.

65. Bao, J. et al., *Optical Properties of Rotationally Twinned InP Nanowire Heterostructures,* Nano Letters **8** (2008) p. 836-841.

66. Vainorius, N. et al., *Confinement in Thickness-Controlled GaAs Polytype Nanodots,* Nano Letters **15** (2015) p. 2652-2656.

67. Joyce, H.J. et al., *Phase Perfection in Zinc Blende and Wurtzite III–V Nanowires Using Basic Growth Parameters,* Nano Letters **10** (2010) p. 908-915.

68. Ikejiri, K. et al., *Zinc Blende and Wurtzite Crystal Phase Mixing and Transition in Indium Phosphide Nanowires,* Nano Letters **11** (2011) p. 4314-4318.

69. Joyce, H.J. et al., *Unexpected Benefits of Rapid Growth Rate for III–V Nanowires,* Nano Letters **9** (2009) p. 695-701.

70. Caroff, P. et al., *Controlled polytypic and twin-plane superlattices in III-V nanowires,* Nature Nanotechnology **4** (2009) p. 50-55.

71. Algra, R.E. et al., *Twinning superlattices in indium phosphide nanowires,* Nature **456** (2008) p. 369-372.

72. Wallentin, J. et al., *Probing the Wurtzite Conduction Band Structure Using State Filling in Highly Doped InP Nanowires,* Nano Letters **11** (2011) p. 2286-2290.

73. Wallentin, J. et al., *Growth of doped InAs$_y$P$_{1-y}$ nanowires with InP shells,* Journal of Crystal Growth **331** (2011) p. 8-14.

74. Noborisaka, J., Motohisa, J., Hara, S., and Fukui, T., *Fabrication and characterization of freestanding GaAs/AlGaAs core-shell nanowires and AlGaAs nanotubes by using selective-area metalorganic vapor phase epitaxy,* Applied Physics Letters **87** (2005) p. 093109.

75. Li, H.Y. et al., *Remote p-Doping of InAs Nanowires,* Nano Letters **7** (2007) p. 1144-1148.

76. Qian, F. et al., *Multi-quantum-well nanowire heterostructures for wavelength-controlled lasers,* Nature Materials **7** (2008) p. 701-706.

77. Zanolli, Z., Pistol, M.-E., Fröberg, L.E., and Samuelson, L., *Quantum-confinement effects in InAs–InP core–shell nanowires,* Journal of Physics: Condensed Matter **19** (2007) p. 295219.

78. Ikejiri, K. et al., *Mechanism of catalyst-free growth of GaAs nanowires by selective area MOVPE,* Journal of Crystal Growth **298** (2007) p. 616-619.

79. Woodruff, J.H. et al., *Vertically Oriented Germanium Nanowires Grown from Gold Colloids on Silicon Substrates and Subsequent Gold Removal,* Nano Letters **7** (2007) p. 1637-1642.

80. Berger, P.R. et al., *Substrate orientation effects on dopant incorporation in InP grown by metalorganic chemical vapor deposition,* Journal of Applied Physics **73** (1993) p. 4095-4097.

81. Kanbe, H., Yamauchi, Y., and Susa, N., *Vapor-phase epitaxial In$_x$Ga$_{1-x}$As on (100), (111)A, and (111)B InP substrates,* Applied Physics Letters **35** (1979) p. 603-605.

82. Rieger, T., Schäpers, T., Grützmacher, D., and Lepsa, M.I., *Crystal Phase Selective Growth in GaAs/InAs Core–Shell Nanowires,* Crystal Growth & Design **14** (2014) p. 1167-1174.

83. Yan, X. et al., *Growth and characterization of InAs quantum dots on InP nanowires with zinc blende structure,* Journal of Vacuum Science & Technology B **31** (2013) p. 051803.

84. Messing, M. et al., *A comparative study of the effect of gold seed particle preparation method on nanowire growth,* Nano Research **3** (2010) p. 506-519.

85. Magnusson, M.H. et al., *Size-selected gold nanoparticles by aerosol technology,* Nanostructured Materials **12** (1999) p. 45-48.

86. Noborisaka, J., Motohisa, J., and Fukui, T., *Catalyst-free growth of GaAs nanowires by selective-area metalorganic vapor-phase epitaxy,* Applied Physics Letters **86** (2005) p. 213102.

87. Dayeh, S.A., Yu, E.T., and Wang, D., *III–V Nanowire Growth Mechanism: V/III Ratio and Temperature Effects,* Nano Letters **7** (2007) p. 2486-2490.

88. Berg, A. et al., *In situ etching for control over axial and radial III-V nanowire growth rates using HBr,* Nanotechnology **25** (2014) p. 505601.

89. Tomioka, K. et al., *Growth of highly uniform InAs nanowire arrays by selective-area MOVPE,* Journal of Crystal Growth **298** (2007) p. 644-647.

90. Ikejiri, K. et al., *Growth characteristics of GaAs nanowires obtained by selective area metal–organic vapour-phase epitaxy,* Nanotechnology **19** (2008) p. 265604.

91. Åberg, I. et al., *A GaAs Nanowire Array Solar Cell with 15.3% Efficiency at 1 Sun*, in *IEEE PVSC* 2015, New Orleans.

92. Yao, M. et al., *GaAs Nanowire Array Solar Cells with Axial p–i–n Junctions,* Nano Letters **14** (2014) p. 3293-3303.

93. Lehmann, S. et al., *A General Approach for Sharp Crystal Phase Switching in InAs, GaAs, InP, and GaP Nanowires Using Only Group V Flow,* Nano Letters **13** (2013) p. 4099-4105.

94. Tomioka, K., Motohisa, J., Hara, S., and Fukui, T., *Crystallographic Structure of InAs Nanowires Studied by Transmission Electron Microscopy,* Japanese Journal of Applied Physics **46** (2007) p. L1102.

95. Motohisa, J. et al., *Catalyst-free selective-area MOVPE of semiconductor nanowires on (111)B oriented substrates,* Journal of Crystal Growth **272** (2004) p. 180-185.

96. Chi, C.-Y. et al., *Twin-Free GaAs Nanosheets by Selective Area Growth: Implications for Defect-Free Nanostructures,* Nano Letters **13** (2013) p. 2506-2515.

97. Gutsche, C. et al., *Controllable p-type doping of GaAs nanowires during vapor-liquid-solid growth,* Journal of Applied Physics **105** (2009) p. 024305.

98. Gutsche, C. et al., *n-Type Doping of Vapor-Liquid-Solid Grown GaAs Nanowires,* Nanoscale Res Lett **6** (2011) p. 65.

99. Borgström, M.T. et al., *Precursor evaluation for in situ InP nanowire doping,* Nanotechnology **19** (2008) p. 445602.

100. Yang, F. et al., *Zn-doping of GaAs nanowires grown by Aerotaxy,* Journal of Crystal Growth **414** (2015) p. 181-186.

101. Tomioka, K., Yoshimura, M., and Fukui, T., *A III-V nanowire channel on silicon for high-performance vertical transistors,* Nature **488** (2012) p. 189-192.

102. Mariani, G. et al., *Patterned Radial GaAs Nanopillar Solar Cells,* Nano Letters **11** (2011) p. 2490-2494.

103. Bryllert, T., Wernersson, L.E., Fröberg, L.E., and Samuelson, L., *Vertical high-mobility wrap-gated InAs nanowire transistor,* Electron Device Letters, IEEE **27** (2006) p. 323-325.

104. Freer, E.M. et al., *High-yield self-limiting single-nanowire assembly with dielectrophoresis,* Nature Nanotechnology **5** (2010) p. 525-530.

105. Tomioka, K. et al., *GaAs/AlGaAs Core Multishell Nanowire-Based Light-Emitting Diodes on Si,* Nano Letters **10** (2010) p. 1639-1644.

106. Colson, P., Henrist, C., and Cloots, R., *Nanosphere Lithography: A Powerful Method for the Controlled Manufacturing of Nanomaterials,* Journal of Nanomaterials **2013** (2013) p. 19.

107. Park, M. et al., *Block Copolymer Lithography: Periodic Arrays of ~10^{11} Holes in 1 Square Centimeter,* Science **276** (1997) p. 1401-1404.

108. Chou, S.Y., Krauss, P.R., and Renstrom, P.J., *Imprint Lithography with 25-Nanometer Resolution,* Science **272** (1996) p. 85-87.

109. Schift, H., *Nanoimprint lithography: An old story in modern times? A review,* Journal of Vacuum Science & Technology B **26** (2008) p. 458-480.

110. Mårtensson, T. et al., *Nanowire Arrays Defined by Nanoimprint Lithography,* Nano Letters **4** (2004) p. 699-702.

111. Hertenberger, S. et al., *High compositional homogeneity in In-rich InGaAs nanowire arrays on nanoimprinted SiO$_2$/Si (111),* Applied Physics Letters **101** (2012) p. 043116.

112. Ji, R. et al., *UV enhanced substrate conformal imprint lithography (UV-SCIL) technique for photonic crystals patterning in LED manufacturing,* Microelectronic Engineering **87** (2010) p. 963-967.

113. Eriksson, T. et al., *High volume nanoimprint lithography on III/V substrates: Imprint fidelity and stamp lifetime,* Microelectronic Engineering **88** (2011) p. 293-299.

114. Javey, A. and Dai, H., *Regular Arrays of 2 nm Metal Nanoparticles for Deterministic Synthesis of Nanomaterials,* Journal of the American Chemical Society **127** (2005) p. 11942-11943.

115. Pierret, A. et al., *Generic nano-imprint process for fabrication of nanowire arrays,* Nanotechnology **21** (2010) p. 065305.

116. Mårtensson, T. et al., *Fabrication of individually seeded nanowire arrays by vapour–liquid–solid growth,* Nanotechnology **14** (2003) p. 1255.

117. Mårtensson, T., *Semiconductor Nanowires: Epitaxy and Applications*, Doctoral Thesis, Department of Physics, Lund University, 2008.

118. Mårtensson, T. et al., *Epitaxial Growth of Indium Arsenide Nanowires on Silicon Using Nucleation Templates Formed by Self-Assembled Organic Coatings,* Advanced Materials **19** (2007) p. 1801-1806.

119. Eklöf, J., *Study and Optimization of Nano Imprinted Surfaces of InP for III-V Nanowire Growth*, Master Thesis, Department of Physics, Lund University, 2013.

120. Stringfellow, G.B., *Thermodynamic aspects of organometallic vapor phase epitaxy,* Journal of Crystal Growth **62** (1983) p. 225-229.

121. Seki, H. and Koukitu, A., *Thermodynamic analysis of metalorganic vapor phase epitaxy of III–V alloy semiconductors,* Journal of Crystal Growth **74** (1986) p. 172-180.

122. Richter, W. et al., *Detailed models of the MOVPE process,* Journal of Crystal Growth **107** (1991) p. 1-11.

123. Johansson, J. et al., *Mass Transport Model for Semiconductor Nanowire Growth,* The Journal of Physical Chemistry B **109** (2005) p. 13567-13571.

124. Dan, D. et al., *Selective-area vapour–liquid–solid growth of InP nanowires,* Nanotechnology **20** (2009) p. 395602.

125. Borg, B.M., Dick, K.A., Eymery, J., and Wernersson, L.-E., *Enhanced Sb incorporation in InAsSb nanowires grown by metalorganic vapor phase epitaxy,* Applied Physics Letters **98** (2011) p. 113104.

126. Fröberg, L.E. et al., *Transients in the Formation of Nanowire Heterostructures,* Nano Letters **8** (2008) p. 3815-3818.

127. Killeen, K.P. and Breiland, W.G., *In situ spectral reflectance monitoring of III-V epitaxy,* Journal of Electronic Materials **23** (1994) p. 179-183.

128. Reinhardt, F. et al., *GaAs surface control during metalorganic vapor phase epitaxy by reflectance anisotropy spectroscopy,* Journal of Vacuum Science & Technology B **11** (1993) p. 1427-1430.

129. Clement, T. et al., *In situ studies of semiconductor nanowire growth using optical reflectometry,* Applied Physics Letters **89** (2006) p. 163125.

130. Tchernycheva, M. et al., *Temperature conditions for GaAs nanowire formation by Au-assisted molecular beam epitaxy,* Nanotechnology **17** (2006) p. 4025.

131. Shin, N. and Filler, M.A., *Controlling Silicon Nanowire Growth Direction via Surface Chemistry,* Nano Letters **12** (2012) p. 2865-2870.

132. Fernández-Garrido, S., Zettler, J.K., Geelhaar, L., and Brandt, O., *Monitoring the Formation of Nanowires by Line-of-Sight Quadrupole Mass Spectrometry: A Comprehensive Description of the Temporal Evolution of GaN Nanowire Ensembles,* Nano Letters **15** (2015) p. 1930-1937.

133. Wang, B. and Leu, P.W., *Tunable and selective resonant absorption in vertical nanowires,* Optics Letters **37** (2012) p. 3756-3758.

134. Anttu, N. and Xu, H.Q., *Efficient light management in vertical nanowire arrays for photovoltaics,* Optics Express **21** (2013) p. A558-A575.

135. Cho, K. et al., *Molecular monolayers for conformal, nanoscale doping of InP nanopillar photovoltaics,* Applied Physics Letters **98** (2011) p. 203101.

136. Wallentin, J. and Borgström, M.T., *Doping of semiconductor nanowires,* Journal of Materials Research **26** (2011) p. 2142-2156.

137. Richter, W. et al., *Orientation dependence of S, Zn, Si, Te, and Sn doping in OMCVD growth of InP and GaAs: application to DH lasers and lateral p-n junction arrays grown on non-planar substrates,* Journal of Crystal Growth **107** (1991) p. 772-778.

138. Perea, D.E. et al., *Direct measurement of dopant distribution in an individual vapour-liquid-solid nanowire,* Nature Nanotechnology **4** (2009) p. 315-319.

139. Dufouleur, J. et al., *P-Doping Mechanisms in Catalyst-Free Gallium Arsenide Nanowires,* Nano Letters **10** (2010) p. 1734-1740.

140. Cui, Y., Duan, X., Hu, J., and Lieber, C.M., *Doping and Electrical Transport in Silicon Nanowires,* The Journal of Physical Chemistry B **104** (2000) p. 5213-5216.

141. Blömers, C. et al., *Hall effect measurements on InAs nanowires,* Applied Physics Letters **101** (2012) p. 152106.

142. Garnett, E.C. et al., *Dopant profiling and surface analysis of silicon nanowires using capacitance-voltage measurements,* Nature Nanotechnology **4** (2009) p. 311-314.

143. Ketterer, B., Uccelli, E., and Fontcuberta i Morral, A., *Mobility and carrier density in p-type GaAs nanowires measured by transmission Raman spectroscopy,* Nanoscale **4** (2012) p. 1789-1793.

144. Khanal, D.R. and Wu, J., *Gate Coupling and Charge Distribution in Nanowire Field Effect Transistors,* Nano Letters **7** (2007) p. 2778-2783.

145. Kim, S.-K. et al., *Tuning Light Absorption in Core/Shell Silicon Nanowire Photovoltaic Devices through Morphological Design,* Nano Letters **12** (2012) p. 4971-4976.

146. Czaban, J.A., Thompson, D.A., and LaPierre, R.R., *GaAs Core–Shell Nanowires for Photovoltaic Applications,* Nano Letters **9** (2009) p. 148-154.

147. Mohan, P., Motohisa, J., and Fukui, T., *Controlled growth of highly uniform, axial/radial direction-defined, individually addressable InP nanowire arrays,* Nanotechnology **16** (2005) p. 2903.

148. Clawson, A.R. and Hanson, C.M., *Tin-doping of n+ InP OMVPE layers,* Journal of Electronic Materials **20** (1991) p. 365-372.

149. ASTM International, *ASTM G173-03(2012), Standard Tables for Reference Solar Spectral Irradiances: Direct Normal and Hemispherical on 37° Tilted Surface.* 2012: West Conshohocken, PA.

150. Shockley, W. and Queisser, H.J., *DETAILED BALANCE LIMIT OF EFFICIENCY OF P-N JUNCTION SOLAR CELLS,* Journal of Applied Physics **32** (1961) p. 510.

151. Luque, A. and Hegedus, S., eds. *Handbook of Photovoltaic Science and Engineering.* Wiley: West Sussex, England. 2003, p. 100.

152. Henry, C.H., *LIMITING EFFICIENCIES OF IDEAL SINGLE AND MULTIPLE ENERGY-GAP TERRESTRIAL SOLAR-CELLS,* Journal of Applied Physics **51** (1980) p. 4494-4500.

153. Nelson, J., *The Physics of Solar Cells*, Imperial College Press: London, 2009, p. 7-8.

154. Green, M.A. et al., *Solar cell efficiency tables (version 46),* Progress in Photovoltaics: Research and Applications **23** (2015) p. 805-812.

155. Nelson, J., *The Physics of Solar Cells*, Imperial College Press: London, 2009, p. 163.

156. Luque, A. and Hegedus, S., eds. *Handbook of Photovoltaic Science and Engineering.* Wiley: West Sussex, England. 2003, p. 105.

157. Luque, A. and Hegedus, S., eds. *Handbook of Photovoltaic Science and Engineering.* Wiley: West Sussex, England. 2003, p. 365-366.

158. Bertness, K.A. et al., *29.5-PERCENT-EFFICIENT GAINP/GAAS TANDEM SOLAR-CELLS,* Applied Physics Letters **65** (1994) p. 989-991.

159. Guter, W. et al., *Current-matched triple-junction solar cell reaching 41.1% conversion efficiency under concentrated sunlight,* Applied Physics Letters **94** (2009) p. 223504.

160. Dimroth, F. et al., *Wafer bonded four-junction GaInP/GaAs//GaInAsP/GaInAs concentrator solar cells with 44.7% efficiency,* Progress in Photovoltaics: Research and Applications **22** (2014) p. 277-282.

161. Yu, S., Kupec, J., and Witzigmann, B., *Efficiency Analysis of III-V Axial and Core-Shell Nanowire Solar Cells,* Journal of Computational and Theoretical Nanoscience **9** (2012) p. 688-695.

162. Fan, Z. et al., *Ordered Arrays of Dual-Diameter Nanopillars for Maximized Optical Absorption,* Nano Letters **10** (2010) p. 3823-3827.

163. Kupec, J., Stoop, R.L., and Witzigmann, B., *Light absorption and emission in nanowire array solar cells,* Optics Express **18** (2010) p. 27589-27605.

164. Nelson, J., *The Physics of Solar Cells*, Imperial College Press: London, 2009, p. 180.

165. Cui, Y. et al., *Efficiency Enhancement of InP Nanowire Solar Cells by Surface Cleaning,* Nano Letters **13** (2013) p. 4113-4117.

166. Hu, Y., Li, M., He, J.J., and LaPierre, R.R., *Current matching and efficiency optimization in a two-junction nanowire-on-silicon solar cell,* Nanotechnology **24** (2013) p. 065402.

167. Kelzenberg, M.D. et al., *Enhanced absorption and carrier collection in Si wire arrays for photovoltaic applications,* Nature Materials **9** (2010) p. 239-244.

168. Bremner, S.P., Levy, M.Y., and Honsberg, C.B., *Analysis of tandem solar cell efficiencies under AM1.5G spectrum using a rapid flux calculation method,* Progress in Photovoltaics: Research and Applications **16** (2008) p. 225-233.

169. Wallentin, J. et al., *Single GaInP nanowire p-i-n junctions near the direct to indirect bandgap crossover point,* Applied Physics Letters **100** (2012) p. 251103.

170. Björk, M.T. et al., *Si–InAs heterojunction Esaki tunnel diodes with high current densities,* Applied Physics Letters **97** (2010) p. 163501.

171. Wallentin, J. et al., *High-Performance Single Nanowire Tunnel Diodes,* Nano Letters **10** (2010) p. 974-979.

172. Wallentin, J. et al., *Degenerate p-doping of InP nanowires for large area tunnel diodes,* Applied Physics Letters **99** (2011) p. 253105.

173. Kempa, T.J. et al., *Single and Tandem Axial p-i-n Nanowire Photovoltaic Devices,* Nano Letters **8** (2008) p. 3456-3460.

174. Kayes, B.M., Atwater, H.A., and Lewis, N.S., *Comparison of the device physics principles of planar and radial p-n junction nanorod solar cells,* Journal of Applied Physics **97** (2005) p. 114302.

175. Chia, A.C.E. and LaPierre, R.R., *Electrostatic model of radial pn junction nanowires,* Journal of Applied Physics **114** (2013) p. 074317.

176. Masatoshi, Y., Eiji, N., Katsuhiro, T., and Takashi, F., *Indium Phosphide Core–Shell Nanowire Array Solar Cells with Lattice-Mismatched Window Layer,* Applied Physics Express **6** (2013) p. 052301.

177. Yoshimura, M., Nakai, E., Tomioka, K., and Fukui, T., *Indium tin oxide and indium phosphide heterojunction nanowire array solar cells,* Applied Physics Letters **103** (2013) p. 243111.

178. Nelson, J., *The Physics of Solar Cells*, Imperial College Press: London, 2009, p. 202.